

Scalable multi-qubit intrinsic gates in quantum dot arrays

Jiaan Qi,^{1,2} Zhi-Hai Liu,¹ and Honqi Xu^{1,2,*}

¹Beijing Academy of Quantum Information Sciences, Beijing 100193, China

²Beijing Key Laboratory of Quantum Devices, Key Laboratory for the Physics and Chemistry of Nanodevices, and School of Electronics, Peking University, Beijing 100871, China[†]

We study multi-qubit quantum gates intrinsic to an array of semiconductor quantum dots and investigate how they can be implemented in a scalable way. The intrinsic quantum gates refer to the class of natural-forming transformations in the qubit rotating-frame under direct exchange coupling, and can be recognized as an instruction set of spin-qubit chips. Adopting perturbative treatment, we can model the intrinsic gates by first-order dynamics in the coupling strength and develop a general formalism for identifying the multi-qubit intrinsic gates under arbitrary array connectivity. The advantageous applications of the intrinsic gates in quantum computing and quantum error correction are explored. Factors influencing the fidelities of the multi-qubit intrinsic gates are also discussed. To overcome the problem of inhomogeneous coupling, we propose a theoretical scheme in which single-qubit pulses are applied to dynamically calibrate the connecting bonds. This scheme can be further combined with periodic dynamical decoupling for robust implementations of multi-qubit gates in large-scale quantum computers.

I. INTRODUCTION

Semiconductor quantum dots are promising physical platforms for universal quantum computing [1–4]. The spins of electrons (or holes) are natural two-level systems that can be selectively manipulated and brought into interactions by confining them with artificial structures. Spin qubits defined in quantum dots enjoy several unique advantages, including their miniature size and compatibility with modern semiconductor fabrication techniques, that make them suitable for creating large-scale quantum chips [5, 6]. Under intensive research efforts from the global community, the technologies and theories behind spin qubits have seen significant advancements over recent years. Continuous developments in key performance metrics such as the coherence times, operation frequencies and gate fidelities have been made [7]. Spin qubits in the state-of-the-art can be prepared and measured with fidelity exceeding 99% [8], manipulated at frequency over 540 MHz [9] and work in temperature above 4K [10]. The fidelity figures for single-qubit and two-qubit gates have been pushed beyond the fault-tolerance threshold value [11, 12]. Industrial manufacturing has also been demonstrated for quantum dot arrays [13, 14].

The natural roadmap of any quantum computing scheme is to incorporate gradually increasing quantities of qubits for realizing useful quantum algorithms. However, accurate control of multiple qubits can be a highly nontrivial task that implies much more than just putting the qubits together. For selective control of the interqubit coupling, the crosstalk effects of the control signals must be suppressed in an efficient manner. In addition, for robust implementation of multi-qubit gates, a method to overcome the inhomogeneous interqubit coupling is also

indispensable. Here the key challenge is that the relevant control resources should scale well with the number of qubits, for potential application to large-scale chips with millions of qubits. For spin qubits, a viable way to scale up the qubit count is to employ an extensible two-dimensional array of quantum dots, as recently demonstrated for crossbar arrays of hole qubits [15–18]. This configuration is also compatible with the surface code, a topological error correction code commonly conceived as the framework for large-scale fault-tolerant quantum computers [19–21]. The ability to control and optimize such a multi-qubit array necessarily marks the next milestone in spin qubits.

The canonical quantum computing theory favors the controlled-not (CNOT) gate as the universal two-qubit gate [22]. Any algorithm may nevertheless be carried out with a different set of universal gates. Analogous to the distinctive basic instruction sets for different classical CPU architectures, quantum computers also have platform-dependent instruction sets. For optimal performance, a quantum algorithm should be compiled into the most natural gates for the physical platform it is applied upon. For spin qubits in particular, we consider a quantum gate as *intrinsic* if it can be attained with a single-step evolution for qubits coupled by exchange interaction only. The controlled-phase (CPhase) or in particular controlled-Z (CZ) gate is an intrinsic two-qubit gate as it can be performed by simply turning on the exchange coupling [23–25]. In comparison, the CNOT gate for spin qubits is not intrinsic by our definition as it relies on external microwave drive to resonantly select the transition states [26]. In general, the “DC control” for CZ gate is less susceptible to noise compared with the “AC control” for CNOT [27–29], and is arguably easier to control and calibrate. Moreover, intrinsic gates need not be limited to two qubits. Most quantum algorithms require imposing joint transformations on multiple qubits. In these scenarios, intrinsic multi-qubit gates can often be used in place of equivalent clusters of single-qubit and

* hqxu@pku.edu.cn

† jiaanq@gmail.com

two-qubit gates. Such replacements can boost efficiency, reducing control expenditures, while also less prone to errors [30]. Giving these obvious benefits, an abundance of recent studies have been devoted to multi-qubit gates in various systems such as Rydberg atoms [31–34], superconducting qubits [30, 35–37] and trapped ions [38, 39]. For spin qubits, the three-qubit Toffoli gate has been proposed and implemented using resonant microwave pulse [40, 41]. Notably, studies on linear quantum dot chains have revealed coherent “superexchange” oscillations of the boundary states [42, 43], and exhibit long-range coupling [44, 45]. These studies clearly demonstrate the possibility of multi-qubit gates with DC control and hint a larger class of intrinsic multi-qubit gates.

Spin arrays coupled by exchange interaction have long fascinated theoretical investigations [46–50]. However, to-date it is still unclear what and how multi-qubit gates can be achieved in general. In this paper, we fill this important gap in current research with a comprehensive study on the qubit dynamics of quantum dot arrays. Extending the theoretical formalisms developed in an earlier paper [51], we greatly generalize the CZ/CPhase gate to a broad class of multi-qubit gates intrinsically accessible to spin qubits. Furthermore, we also show these multi-qubit gates are scalable by proposing an efficient theoretical scheme to dynamically calibrate and control the inter-qubit couplings. While minimizing the crosstalk problem for selective controls, our scheme can also simultaneously protect the qubits from environmental couplings. Hopefully, our findings can pave the way for future large-scale quantum computing using spin qubits.

This paper is organized as follows. Section II goes through the theoretical prerequisites for the study of intrinsic gates. These include the entangled-state representation of the effective Hamiltonian, followed by introduction of the qubit frame, where quantum gates are formally derived and extended with additional free phase gates. In section III, we look into the class of all possible multi-qubit intrinsic gates defined on a quantum dot array with any geometry. It turns out that there is a surprisingly easy way of decomposing them. We estimate the coherent fidelity of these multi-qubit gates and discuss their potential applications in quantum computation and quantum error correction. In section IV, we examine the unavoidable problem of inhomogeneous coupling brought by scaling up the system. We propose a theoretical scheme to dynamically calibrate the bonds by applying single-qubit pulses. These scheme can be further combined with various dynamical decoupling protocols [52–54] in a suitable way that protect the spin qubits from environmental noise. Finally, we discuss a technical prospect implied by our theory where the interdot coupling can be efficiently controlled by tuning the local spin-orbital coupling strength. We summarize and conclude in section V.

II. DYNAMICS OF THE DOT ARRAY

A. Entangled state representation of the effective Hamiltonian

The quantum chip for our study is a semiconducting nanostructure featuring an array of quantum dots. The dots can be typically arranged in 1 or 2 spatial dimensions and we use the word “array” irrespective of dimensionality. The dot array is kept at low temperature and has a suitable confining potential such that free charge carriers (electrons or holes) are captured in the half-filling regime, i.e., only a single carrier occupies each dot. To define spin qubits associated with the dots, a static magnetic field is applied to the system, lifting the spin degeneracy of the ground-level orbits. These dots can have different local Landé g -factor tensors, hence the spatial quantization axes and Zeeman splitting energies for each dot can differ. This device also possesses considerable spin-orbital interaction (SOI) to enable fast manipulation of spin states with electric signals [55]. The SOI can be either intrinsic to the nanostructure [56] or artificially introduced by slanting magnetic field [57]. An example set up is illustrated in Fig. 1(a) for a two-dimensional grid of quantum dots.

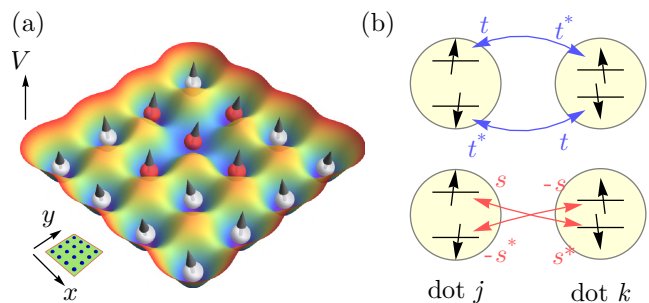


FIG. 1. (a) The potential profile of a two-dimensional array of quantum dots serving as a prototypical spin qubit quantum chip (left-bottom inset). Localized charge carriers with spins are represented as small balls with arrows. The red balls are in an active region where multiple spins are simultaneously coupled together for a multi-qubit gate. (b) Schematic plot of the spin qubits and the interdot coupling through virtual tunneling. Each qubit is defined by the lowest-energy spin-split states localized to a dot. The coefficients representing 8 possible tunneling processes can be reduced to only two complex numbers due to symmetry—the spin conserved tunnelling t and spin-flipped tunnelling s .

The Fermi-Hubbard model is a good starting point for describing such quantum dot array [58, 59]. The low-energy states localized to all the dots can be normalized to form a basis $\{|\Phi_{j\sigma}\rangle\}$, where j represents the dot location and $\sigma \in \{\uparrow, \downarrow\}$ is the spin index. Introducing the annihilation $a_{j\sigma}$ and creation $a_{j\sigma}^\dagger$ operators for the basis states, one can write down a second-quantized Hamiltonian that consists of a “dot” part H_{dot} and a “tunneling” part H_{tun} . The dot part describes the energy cost for fill-

ing 0 to 2 charge carriers into the ground-level orbit of each quantum dot,

$$H_{\text{dot}} = \sum_{j\sigma} \left[(\mu_j + \text{sig}(\sigma_j) \frac{1}{2} \varepsilon_j^Z) n_{j\sigma} + \frac{1}{2} U_j n_{j\sigma} n_{j\bar{\sigma}} \right], \quad (1)$$

where $n_{j\sigma} = a_{j\sigma}^\dagger a_{j\sigma}$ is the number operator for the σ spin state at dot j , μ_j and ε_j^Z are the local chemical potential and the Zeeman splitting energy at dot j , the spin sign is defined by $\text{sig}(\uparrow\downarrow) = \pm 1$ and U_j is the Coulomb charging energy for filling two antiparallel spins into the same dot j . Interdot tunneling of charge carriers is described by

$$H_{\text{tun}} = \sum_{\langle j,k \rangle} \sum_{\sigma} \left(t_{\sigma\sigma}^{jk} a_{j\sigma}^\dagger a_{k,\sigma} + t_{\sigma\bar{\sigma}}^{jk} a_{j\sigma}^\dagger a_{k,\bar{\sigma}} \right), \quad (2)$$

where the first summation is over all pairs of neighboring dots $\langle j,k \rangle$ that can be coupled via electronic tunneling, $t_{\sigma\sigma}^{jk}$ and $t_{\sigma\bar{\sigma}}^{jk}$ represent the spin dependent tunneling coefficients between adjacent dots j,k . Examining the tunneling process among a pair of dots j and k , we can identify four spin-conserved terms in addition to four spin-flipped terms. The spin-flipping can be attributed to differences in the local quantization axes, and/or the SOI effects of the structure [60, 61].

A necessary assumption for our theory is that the typical Zeeman energy associated with each dot is much smaller than the potential barrier between the dots. As explained in the Appendix A 2, this assumption translates to a weak time reversal symmetry condition that allows the tunneling coefficients to be reduced into only two complex numbers,

$$\begin{aligned} t_{\uparrow\uparrow}^{jk} &= (t_{\downarrow\downarrow}^{jk})^* = t_{\downarrow\downarrow}^{kj} = (t_{\uparrow\uparrow}^{kj})^* && \equiv t_{jk} \propto \tilde{t}_{jk} \\ t_{\downarrow\downarrow}^{jk} &= -(t_{\uparrow\uparrow}^{jk})^* = -t_{\uparrow\uparrow}^{kj} = (t_{\downarrow\downarrow}^{kj})^* && \equiv s_{jk} \propto \tilde{s}_{jk}. \end{aligned} \quad (3)$$

where we have introduced the spin-conserved (t_{jk}) and the spin-flipped (s_{jk}) tunneling coefficients. This relation among tunneling coefficients is illustrated in Fig. 1(b). For convenience, we also introduce the dimensionless tunneling coefficients \tilde{t}_{jk} and \tilde{s}_{jk} , that are normalized to unity $|\tilde{t}_{jk}|^2 + |\tilde{s}_{jk}|^2 = 1$. In particular, for systems where the g -factors are scalar, we can further derive the explicit parametrization $\tilde{t} = \cos(\gamma_{\text{SOI}}) + i \sin(\gamma_{\text{SOI}}) \cos(\vartheta_{\text{B}})$ and $\tilde{s} = i \sin(\gamma_{\text{SOI}}) \sin(\vartheta_{\text{B}})$, where γ_{SOI} and ϑ_{B} characterize the SOI strength and the effective magnetic field angle in the vicinity of a pair of dots (dot-subscripts omitted here) [51]. These relations suggest it is possible to experimentally control the portion of spin-conserved and spin-flipped coefficients by varying the SOI strength and/or magnetic field angle.

The immediate state after tunneling involves two spins occupying the same dot and is not energetically favored due to the large Coulomb repulsion energy. The theory of quantum mechanics, however, allows brief transition to such high energy states. This virtual tunneling process gives rise to direct exchange interaction, assumed to

be the main interqubit coupling mechanism for our device. To specify the dynamics of the half-filling states of interest, we introduce the computational basis states for an array of N_Q quantum dots,

$$|n\rangle \equiv |\sigma_{n_1}, \sigma_{n_2}, \dots, \sigma_{n_{N_Q}}\rangle, \quad \text{for } n = 1, 2, \dots, 2^{N_Q}, \quad (4)$$

where the component $\sigma_{n_j} \in \{\uparrow, \downarrow\}$ is the spin state at dot j and n_j can be viewed as the binary digit of n . Each $|n\rangle$ is an Fermionic (antisymmetric) multi-body wave function and Eq. (4) can be viewed as a Fock space representation from a formal point of view.

The tunneling coefficients for a pair of connected dots $w = \langle j,k \rangle$ can be used to specify an entangled state that lives on the four-dimensional space spanned by the half-filling states of the connecting dots,

$$|\xi_w\rangle = \frac{1}{\sqrt{2}} \left(\tilde{s}_w |\uparrow\uparrow\rangle_w - \tilde{t}_w |\uparrow\downarrow\rangle_w + \tilde{t}_w^* |\downarrow\uparrow\rangle_w + \tilde{s}_w^* |\downarrow\downarrow\rangle_w \right). \quad (5)$$

With this entangled state defined, the rule to write down the computational Hamiltonian is handy,

$$H = \underbrace{\sum_j \frac{1}{2} \varepsilon_j^Z \sigma_j^Z}_{H_{\text{qu}}} - \underbrace{\sum_{w=\langle j,k \rangle} J_w |\xi_w\rangle \langle \xi_w|}_{H_{\text{ex}}}, \quad (6)$$

where the first part H_{qu} defines the energy splitting of the qubits, which is the summation of the effective Zeeman splitting energies ε_j^Z along the Pauli operator $\sigma_j^Z = |\uparrow\rangle\langle\uparrow|_j - |\downarrow\rangle\langle\downarrow|_j$ for all dots. The exchange term H_{ex} describes the coupling among connecting dots (edges/bonds), with coupling strength specified by the exchange energy,

$$J_{jk} = \frac{|t_{jk}|^2 + |s_{jk}|^2}{2} \left(\frac{1}{U_j + \mu_j - \mu_k} + \frac{1}{U_k + \mu_k - \mu_j} \right). \quad (7)$$

We provide an explicitly derivation of this result in Appendix A. However, one can show that these two representations are equivalent.

Equation (6) represents the effect of direct exchange in terms entangled states that live on connected edges. This is quite distinctive from the traditional representation of the exchange interaction $H_{\text{ex}} = \mathbf{S}_j \mathcal{J}_{jk} \mathbf{S}_k$, where \mathcal{J}_{jk} is generally a tensor. Besides being mathematically compact, our entangled-state representation allows easier treatment of the anisotropic exchange and has many nice properties that we will take advantage of in the development of multi-qubit gates.

B. Time evolution in the qubit frame

For any quantum computing system, the Hamiltonian governing qubit dynamics can be split as $H = H_0 + H_I$, where H_0 is the intrinsic Hamiltonian (self-energy) for proper definition of qubits; H_I includes the external control and internal coupling necessary for manipulation of

the register states. H_0 is typically static and induces the unitary transform $U_0(\tau) = e^{-iH_0\tau}$ to the lab-frame states. This constant rotation defines the qubit frame and qubit states. A quantum gate is a linear map among qubit states. It is implemented by the qubit-frame time evolution $\tilde{U}(\tau)$ generated by $\tilde{H}_1(\tau) = U_0(\tau)^\dagger H_1 U_0(\tau)$. Usually, the time-dependence in $\tilde{H}_1(\tau)$ makes time integration difficult to solve analytically. We can take an equivalent approach by reversely rotating the qubit frame and express $\tilde{U}(\tau)$ as the product

$$\tilde{U}(\tau) = e^{+i\tau H_0} e^{-i\tau(H_0+H_1)}. \quad (8)$$

We note that one cannot cancel the H_0 terms, which would require H_0 and H_1 to commute. For the spin-qubit chip hosted on a multi-dot array, we set $H_0 = H_{\text{qu}}$ and $H_1 = H_{\text{ex}}$, as naturally suggested by Eq. (6). It is also possible to use the external microwave frequency to define similar rotating frame, but such choice would be problematic if multiple qubits with different Zeeman energies are involved [62].

To proceed with the qubit-frame time evolution, we make the assumption that the typical Zeeman energy is much larger than the typical interdot exchange energy $\varepsilon^Z \gg J$ in the device working regime. Notably, this condition suggests $\|H_{\text{qu}}\| \gg \|H_{\text{ex}}\|$ and allows the Hamiltonian $H = H_{\text{qu}} + H_{\text{ex}}$ to be approached in a perturbative way. It is obvious from Eq. (6) that the H_{qu} eigenstates are just $\{|n\rangle\}$, with corresponding eigenenergies

$$E_n = \sum_n \frac{1}{2} \text{sig}(\sigma_{n_j}) \varepsilon_j^Z. \quad (9)$$

Let us denote the eigenstates and eigenenergies of H as $\{|n'\rangle\}$ and $\{E'_n\}$, which are perturbed from the eigenstates $\{|n\rangle\}$ and eigenenergies $\{E_n\}$ of H_{qu} . The matrix exponential of H_0 and H for $\tilde{U}(\tau)$ can be taken under the respective eigen-basis $\{|n\rangle\}$ and $\{|n'\rangle\}$. In particular, the diagonal elements of $\tilde{U}(\tau)$ can be found by

$$\langle n | \tilde{U}(\tau) | n \rangle = r_{nn} e^{-i\tau \delta E_n} + \sum_{m \neq n} r_{nm} e^{-i\tau(E'_m - E_n)}, \quad (10)$$

where $r_{nm} \equiv |\langle n | m' \rangle|^2$ and $\delta E_n \equiv E'_n - E_n$. While the expression for Eq. (10) is exact, the perturbative assumption suggests that it consists of a major term with $r_{nn} \sim 1 - O(J^2)$, and a summation of minor terms with $r_{nm} \sim O(J^2)$, for $m \neq n$. As a result, we construct the following ‘‘ideal’’ gate $\tilde{U}_{\text{ideal}} \approx \tilde{U}$, where only the first-order effects are kept,

$$\tilde{U}_{\text{ideal}} \equiv \text{diag}(e^{-i\tau \delta E_1^{(1)}}, e^{-i\tau \delta E_2^{(1)}}, \dots, e^{-i\tau \delta E_d^{(1)}}), \quad (11)$$

where $\delta E_n^{(1)} = \langle n | H_{\text{ex}} | n \rangle \sim O(J)$ is the first order energy correction for the n th level. In this sense, we can view the intrinsic gates on quantum dot arrays as the first-order dynamical effects of the exchange coupling. In comparison, the zeroth-order term defines the qubit

Hilbert space, while all the higher-order terms are attributed as errors.

We should remark that the identity $\delta E_n^{(1)} = \langle n | H_{\text{ex}} | n \rangle$ is a result of non-degenerate perturbation theory, where the E_n values are assumed to be distinctive. Thus it is tempting to also impose the requirements $|E_n - E_m| > \|H_{\text{ex}}\|$ for all n, m . However, such constraints are neither practical for large-scale systems nor necessary for the definition of \tilde{U}_{ideal} . The difference between $\tilde{U}(\tau)$ and \tilde{U}_{ideal} is viewed as a source of *coherent* error in gate implementation. In the case of near-degenerate E_n values, the perturbative series converges slowly and approximating $\tilde{U}(\tau)$ by \tilde{U}_{ideal} will necessarily result in large error. We will estimate the coherent error and the suppression of it in further details in Sec. III C. For the most part of this paper, we focus on what and how a useful quantum gate can be achieved with \tilde{U}_{ideal} .

C. Grid and bond vectors

By definition, \tilde{U}_{ideal} is diagonal in the computational basis. Therefore a convenient way to express the \tilde{U}_{ideal} is to introduce

$$\tilde{U}_{\text{ideal}} = e^{i\tau \mathbf{\Lambda}}, \quad (12)$$

where $\mathbf{\Lambda}$ is the diagonal matrix defined by the first-order energy corrections, or simply a vector of diagonal elements when its clear from the context. Using first-order perturbation theory, we can explicitly derive

$$\mathbf{\Lambda} = \bigoplus_w J_w \text{diag}(|\xi_w\rangle\langle\xi_w|) \equiv \bigoplus_w \mathbf{\Lambda}_w, \quad (13)$$

where the Kronecker sum (\oplus) is defined for vectors (matrices) $\mathbf{x} \in A$ and $\mathbf{y} \in B$ in different linear spaces by, $\mathbf{x} \oplus \mathbf{y} = \mathbf{x} \otimes \mathbf{1}_{B \setminus A} + \mathbf{1}_{A \setminus B} \otimes \mathbf{y}$, where $\mathbf{1}_{B \setminus A}$ is the one-vector (or identity matrix) on the difference space $B \setminus A$, and vice versa for $\mathbf{1}_{A \setminus B}$. As $\mathbf{\Lambda}$ depends on all connecting edges of the quantum-dot array while $\mathbf{\Lambda}_w$ depends only on a particular bond, we refer the former as the ‘‘grid vector’’ and later as the ‘‘bond vector’’. Each bond vector can be explicitly represented in its associated 4-dimensional subspace by

$$\begin{aligned} \mathbf{\Lambda}_w &\hat{=} (\frac{1}{2}J_w|s_w|^2, \frac{1}{2}J_w|t_w|^2, \frac{1}{2}J_w|t_w|^2, \frac{1}{2}J_w|s_w|^2) \\ &\equiv (S_w, T_w, T_w, S_w) \end{aligned} \quad (14)$$

where we have introduced the shorthands S_w and T_w for the spin-conserved and spin-flipped tunneling strengths.

Despite the simple form of each bond vector, it can be quite involved to calculate the Kronecker sum of all bonds in a large grid. The vector components of $\mathbf{\Lambda}$ are summations of different S_w and T_w terms. Their exact expressions depend on the order of qubits and the connectivity of the full grid, and there can have many possible ways of connection for a large collection of quantum dots. However, thanks to the structure of the each bond

vector, one can show that the grid vector always satisfies the reflective symmetric condition

$$\mathbf{\Lambda} = \overleftarrow{\mathbf{\Lambda}} \equiv (\overrightarrow{\mathbf{\lambda}}, \overleftarrow{\mathbf{\lambda}}), \quad (15)$$

where we introduce the right and left over-arrow to represent writing a vector in normal and reserve order respectively. For an N_Q -qubit system, the length of $\mathbf{\Lambda}$ is 2^{N_Q} while the length of $\mathbf{\lambda}$ is 2^{N_Q-1} . This property implies that there are at most one-half independent entries in $\mathbf{\Lambda}$, defined by the *reduced* grid vector $\mathbf{\lambda}$.

D. Free phase factors

The DC time evolution under anisotropic exchange is responsible for entangling different spin qubits. To convert the time evolution map into more familiar expressions of quantum gates, we allow additional global phase and local phase gates. We refer these combined phase degrees of freedom as the free phase factors.

Firstly, a global phase factor can be applied to any wave vector without inducing conceivable change of any physical observables. Hence two unitary maps related by an arbitrary global phase factor ϕ_g are completely equivalent, $e^{i\phi_g}U \doteq U$, where the dot-equal symbol is used to represent such equivalence. More importantly, we also allow two unitary gates to differ by local phase gates on individual qubits. The rationale behind such local phase freedom is that Z -axis rotations can be implemented by the so-called virtual- Z gates in the software level and do not require actual operations on the qubits [62, 63]. This local phase freedom is also exploited in original the proposal of two-qubit CZ gate [23]. In this paper, we will assume that such single-qubit Z rotations come at trivial cost of state fidelity or operation time. The phase gate for a single qubit is the operator $Z_\phi = e^{-i(\phi/2)\sigma_z} \doteq \text{diag}(1, e^{i\phi})$. Direct product of single qubit phase gates gives local phase gates for multi-qubits. Combing the global and local phase degree of freedom, we can define a free phase map

$$Z_{\text{free}} \equiv e^{i\phi_g} \bigotimes_j Z_{\phi_j} = e^{i\Phi_F}, \quad (16)$$

where we can associate Z_{free} with a vector Φ_F , as all phases gates are diagonal. The ‘‘free vector’’ Φ_F is a sum of a global phase and a local part $\Phi_F = \phi_g + \Phi_{\text{loc}}$, with the local free vector

$$\Phi_{\text{loc}} \equiv \bigoplus_j (0, \phi_j). \quad (17)$$

We say that a multi-qubit gate G can be intrinsically attained under direct exchange if it is related to the qubit-frame operator \tilde{U}_{ideal} up to free phase factors,

$$\tilde{U}_{\text{ideal}}(\tau_G) = Z_{\text{free}}(\phi_G) G, \quad (18)$$

where ϕ_G is the solution of (global and local) phase factors and τ_G is the time duration for implementing gate G . As both \tilde{U}_{ideal} and Z_{free} are diagonally represented in the computation basis, we are interested in the multi-qubit gates that are also diagonal in the computational space. The unitarity requirement of such gate G implies that the diagonal elements of G are all just phase factors and can be written as

$$G = e^{i\Theta_G}, \quad (19)$$

where the gate vector Θ_G consists of real numbers associated with the gate. Focusing only on the phase factors, we obtain from Eqs. (11, 16, 19) the relation for the vectors,

$$\tau\mathbf{\Lambda} = \Theta_G + \Phi_F \pmod{2\pi}, \quad (20)$$

where the equality is understood in terms of 2π modulus in all the vector components as any extra 2π phase factor contributes trivially.

III. INTRINSIC MULTI-QUBIT GATES

Equipped with the Hamiltonian and phase corrections, in this section we study what multi-qubit gates can be intrinsically achieved on a general spin-qubit grid. We will first consider some specific examples and their potential applications then develop a general theory for identifying the intrinsic quantum gates.

A. Multi-qubit controlled-phase gates

A particular useful class of quantum gates is the general controlled-phase gates. We require these gates to involve at least one control qubit and at least one target qubit subjecting to phase-shift according to the state of the control qubit(s). Notable examples include the regular controlled- Z (CZ), the Toffoli-type controlled-controlled- Z (CCZ) and the parity checker controlled- Z - Z (CZZ) gate. Here we will examine of what gates are achievable and in what kind of geometry can it be achieved.

1. Composition rules

Without loss of generality, we fix the first qubit as the control qubit and label it by ‘C’, with the rest qubits, which may or may not be involved in the gate, labelled by $1, 2, \dots, n \equiv N_Q - 1$. Setting the first qubit as control implies that the first half of the computational states remain intact under the gate transformation, while the second half is subject to certain phase flips. Therefore the gate vector of such gate can be written as

$$\Theta_G = (\mathbf{0}, \theta_G), \quad (21)$$

where the zero vector $\mathbf{0}$ has half the length of Θ_G and we refer the vector θ_G as the reduced gate vector.

For the above specified qubit labels, the local phase factors comprise a vector $\phi_{\text{loc}} = (\phi_C, \phi_1, \dots, \phi_n) = (\phi_C, \phi_T)$. Note that we use capital and lower-case letter to distinguish the local free vector with the vector of local phase factors. Expanding the free vector over the control qubit according to Eq. (17), we find $\Phi_{\text{loc}} = (\Phi_T, \phi_C + \Phi_T)$, where Φ_T is the free phase vector for ϕ_T only. To further take advantage of the property that the vector Λ is reflectively symmetric, we split all vectors in Eq. (20) into equal halves and equate them separately. This allows us to formulate two equivalent gate composition rules in terms of the reduced phases vectors. An intrinsic gate must satisfy both rules simultaneously. The first is the *parity rule*,

$$\theta_G = \overleftarrow{\Phi}_T - \overrightarrow{\Phi}_T - \phi_C = L_{N_Q} \phi_{\text{loc}} \pmod{2\pi}, \quad (22)$$

where we have introduced the parity matrix L_{N_Q} that is uniquely determined by the total number of qubits N_Q . Since θ_G is 2^{N_Q-1} dimensional but there are only N_Q local phases to vary, a large number of gates are rejected by the parity rule. The parity rule thus offers a straightforward way to examine whether a gate is allowed or not in theory. After solving the required local phase corrections, the next step is to examine the *dynamics rule*,

$$\tau \lambda = \phi_g + \Phi_T \pmod{2\pi}, \quad (23)$$

with Φ_T determined by Eq. (22). This equation connects the required local phase corrections to the grid vector. Therefore it determines what type of connectivity of the quantum dots is required for implementing a target gate within finite time.

2. Examples

At this stage, it is helpful to first examine some simple examples of quantum gates.

The simplest case is a two-qubit system. It is well-known that DC evolution under exchange can produce the CZ gate. Here we examine the general controlled-phase gate $\text{CZ}_\theta \hat{=} \text{diag}(1, 1, 1, e^{i\theta})$. The parity rule for such gate reads

$$\begin{pmatrix} 0 \\ \theta \end{pmatrix} = \begin{pmatrix} -1 & 1 \\ -1 & -1 \end{pmatrix} \begin{pmatrix} \phi_C \\ \phi_1 \end{pmatrix} \pmod{2\pi}. \quad (24)$$

Since the parity matrix is invertible, any θ value is allowed. The general solution of local phase factors is given by $\phi_1 = -\frac{1}{2}\theta + k_1\pi$ and $\phi_C = -\frac{1}{2}\theta + (k_1 + 2k_2)\pi$ for $k_1, k_2 \in \mathbb{Z}$. As there is only one possible way of connecting two dots, the reduced grid vector is identified by $\lambda = (S, T)$. Substituting into the dynamics rule, we can obtain the explicit gate time,

$$\tau = \frac{-\theta/2 + n\pi}{T - S}, \quad n \in \mathbb{Z}. \quad (25)$$

Here the integer n is further restricted such at $\tau > 0$.

Increasing the qubit number to three, we have a much more interesting system that can demonstrate many interesting aspects of multi-qubit gates. We first explicitly write down the parity rule for three-qubit gates,

$$\theta_G = \begin{pmatrix} -1 & 1 & 1 \\ -1 & 1 & -1 \\ -1 & -1 & 1 \\ -1 & -1 & -1 \end{pmatrix} \begin{pmatrix} \phi_C \\ \phi_1 \\ \phi_2 \end{pmatrix} \pmod{2\pi}. \quad (26)$$

The parity matrix is 4×3 . This indicates there are more constraints than the free local phase variables. Hence only a subset of the three-qubit controlled phase can be intrinsically implemented. A striking example prohibit by parity is the CCZ gate. It corresponds to the gate vector $\theta_G = (0, 0, 0, \pi)$. Substituting θ_G into the above equation, we obtain

$$\begin{cases} -\phi_C + \phi_1 + \phi_2 = 2n\pi \\ \phi_C - \phi_1 + \phi_2 = 2m\pi \\ \phi_C + \phi_1 - \phi_2 = 2k\pi \\ \phi_C + \phi_1 + \phi_2 = 2l\pi - \pi \end{cases}, \quad (27)$$

where n, m, k, l are integers. Summing up the first three terms yield the final term on the left-hand-side, but the right-hand-sides suggests the sum is simultaneously even and odd multiple of π , an apparent contradiction.

A class of achievable gate is the $\text{CZ}_{\theta_1} \text{Z}_{\theta_2}$, which applies conditional phase shifts of θ_1 and θ_2 for qubit 1 and 2. Plugging in the corresponding gate vector $\theta_G = (0, \theta_2, \theta_1, \theta_1 + \theta_2)$ into Eq. (26), one can verify that a consistent solution can be found by

$$\begin{cases} \phi_1 = -\frac{1}{2}\theta_1 + k_1\pi \\ \phi_2 = -\frac{1}{2}\theta_2 + k_2\pi \\ \phi_C = -\frac{1}{2}\theta_1 - \frac{1}{2}\theta_2 + (k_1 + k_2 + 2k_3)\pi \end{cases}, \quad (28)$$

where k_1, k_2, k_3 are arbitrary integers. From local phase solutions, we can determine $\Phi_T = (0, \phi_2, \phi_1, \phi_1 + \phi_2)$. Next, we also need to check if such gate is dynamically allowed. For a three-qubit system, there can have three distinct bonds in the fully-connected setup. And this generalize to $\binom{n}{2}$ bonds in a fully-connected n -qubit system. But here we only consider a one-dimensional array with two connecting bonds. And we can distinguish two possibilities for a three-qubit system—that of linear fashion, where the control and target qubits are connected sequentially in the order of ‘C’-‘1’-‘2’; and the that of stellar fashion, in which the control qubit is placed in the center following ‘1’-‘C’-‘2’. For the stellar geometry, the grid vector can be calculated as

$$\lambda^{(\text{ste})} = (S_1 + S_2, S_1 + T_2, S_2 + T_1, T_1 + T_2). \quad (29)$$

Substituting the grid vectors into Eq. (22), we find that the dynamics condition decouples to separate identities for each bond:

$$\tau(T_1 - S_1) = \phi_1, \quad \tau(T_2 - S_2) = \phi_2, \quad \pmod{2\pi}. \quad (30)$$

This can be in principle achieved by controlling the tunneling ratio $(T_1 - S_1)/(T_2 - S_2)$. On the other hand, the linear geometry is associated with

$$\boldsymbol{\lambda}^{(\text{lin})} = (S_1 + S_2, S_1 + T_2, T_1 + T_2, S_2 + T_1). \quad (31)$$

Contrary to the previous case, there is no non-trivial solution to the dynamics rule, unless if $\phi_2 = \pi \pmod{2\pi}$. But this would indicate that qubit 2 undergoes a conditional 2π rotation, which is equivalent to a Z gate on the control qubit, and the resulting gate reduces to a two-qubit gate. In particular, if the two bonds are identical, then after time $\tau = \pi/(T - S)$, we have $\phi_c = \phi_2 = \pi$ and $\phi_1 = 0$, the locally-uncorrected time evolution will become joint single-qubit Z gates on both ends:

$$\tilde{U}(\tau) = Z_c \otimes Z_2, \quad (32)$$

which is a non-entangling gate even though the qubits are entangled amidst the time evolution.

3. General multi-qubit control gates

A particular class of quantum gates is naturally allowed by parity. This class has only one control qubit but allow multiple target qubits, $CZ_{\theta_1} Z_{\theta_2} \cdots Z_{\theta_n}$. In particular, when all controlled-phase factors are π , these become the multi-qubit controlled- Z gates, which have important application in quantum computing algorithms and quantum error correction codes. For such multi-qubit controlled-phase (MQCP) gate, we have the reduced gate vector $\boldsymbol{\theta}_G = (0, \theta_1) \oplus (0, \theta_2) \oplus \cdots \oplus (0, \theta_n)$. After calculating the target free vector and its reverse vector by Eq. (17), we obtain the parity rule

$$\bigoplus_{j=1}^n (0, \theta_j) = \bigoplus_{j=1}^n (\phi_j, -\phi_j) - \phi_c \pmod{2\pi}. \quad (33)$$

for which we have the solution

$$\begin{cases} \phi_j = -\frac{1}{2}\theta_j \pmod{\pi} \\ \phi_c = \sum_{j=1}^n \phi_j \pmod{2\pi} \end{cases}. \quad (34)$$

This explicitly proves that such one-control, multi-target gate is allowed by parity.

In comparison, the parity rule requires that the number of control qubits cannot exceed 1. This is already hinted by the three qubit example. We formally prove this theorem in the follows. Without loss of generality, we set the qubit 1 also as the control qubit. This implies that such $\boldsymbol{\theta}_G = (\mathbf{0}, \boldsymbol{\theta}'_G)$, where $\mathbf{0}$ is a zero vector of length 2^{n-1} . Next, we partition both sides of the parity rule into equal halves, yielding

$$\begin{cases} \phi_1 - \phi_c + \bigoplus_{j=2}^n (\phi_j, -\phi_j) = \mathbf{0} \\ -\phi_1 - \phi_c + \bigoplus_{j=2}^n (\phi_j, -\phi_j) = \boldsymbol{\theta}'_G \end{cases} \pmod{2\pi} \quad (35)$$

Solving this condition, we find the vector $\boldsymbol{\theta}'_G = -2\phi_1$ a constant vector (up to 2π modulus). But such solution in turn suggest that the gate is a controlled-phase between C and 1 instead of a multi-qubit gate with two control qubits, which completes our proof. For this reason, we will only consider the gates with one control qubit when taking about multi-qubit control.

Let us now examine the the dynamics rule for the multi-qubit control gate. As hinted by the three qubit example, it turns out that such gate can be generally implemented in a stellar geometry. In the stellar geometry, the control qubit lives in the center of a cluster, and all other qubits are directly connected to the control qubit via bonds $1, 2, \dots, n$. The reduced grid vector in such case can be worked out as

$$\boldsymbol{\lambda}^{(\text{ste})} = (S_1, T_1) \oplus (S_2, T_2) \oplus \cdots \oplus (S_n, T_n). \quad (36)$$

Substituting the $\boldsymbol{\lambda}$ vector into Eq. (23), we require

$$\bigoplus_j (\tau S_j, \tau T_j) = \phi_g + \bigoplus_j (0, \phi_j), \quad (37)$$

which can be solved by taking $\phi_g = \sum \tau S_j$ and that each bond satisfying

$$\tau(T_j - S_j) = \phi_j = -\frac{1}{2}\theta_j \pmod{\pi}. \quad (38)$$

This solution suggests that such multi-qubit control is also allowed dynamically. This completes the full proof that the multi-qubit controlled phase gates are intrinsic. Of course, we have hitherto only considered the theoretical perspectives and leave out the technical details. From Eq. (38), we see that arbitrary controlled phases can be in principle achieved by controlling the tunnelling strength T_j and S_j for each bond. But as the qubit number scales up, the resources for simultaneously calibrating and controlling all bonds quickly become unmanageable. We will discuss a more robust and scalable scheme to fulfill this dynamics condition in Section IV.

We can also examine the multi-qubit controlled-phase under another type of geometry—the linear geometry. In the linear geometry, the qubits are labeled sequentially from one end to another end of an 1D chain (in a topologically equivalent way), and are connected with near-neighbors. A general multi-qubit controlled-phase gate cannot be implemented in the linear geometry. But there is one exception: For a homogeneous chain with one control and n target qubits, a π -phase can accumulate on both ends $\phi_c = \phi_n = \pi$ but coherently cancels out for other qubits $\phi_1 = \phi_2 = \cdots \phi_{n-1} = 0$. Such solution is already discussed in the three-qubit example. We can prove the general case with mathematical induction by noting the following recurrence relation

$$\boldsymbol{\lambda}^{(n+1)} = \boldsymbol{\lambda}^{(n)} \otimes (1, 1) + \boldsymbol{\lambda}^{(n-1)} \otimes (S, T, T, S), \quad (39)$$

where $\boldsymbol{\lambda}^{(n)}$ is the the grid vector for chains with n target qubits. In such case, the solutions to the dynamics rule

exist at

$$\tau = \frac{(2k+1)\pi}{T-S}, \quad k \in \mathbb{Z}. \quad (40)$$

The resulting uncorrected time evolution is simply

$$\tilde{U}(\tau) = Z_c \otimes I_1 \otimes I_2 \otimes \cdots \otimes I_{n-1} \otimes Z_n. \quad (41)$$

We remark that the superexchange oscillations observed for boundary states of a spin chain are manifestation of this gate [42, 43]. Such gate might be trivial from the quantum computational perspective, as it is just joint single-qubit Z . But the underlying physics is quite interesting. The final gate does not depend on the shape and number of qubits involved in the path connecting the control and the final target qubit. In other words, it has the property of being topologically invariant.

B. General gate decompositions

The MQCP gates stand for only a small fraction of what can be intrinsically achieved on a multi-qubit array. And there can be many different intrinsic gates under different types of dot connectivity. But it turns out that all the intrinsic gates can be decomposed into simultaneous MQCP gates. As a result, all the conclusions regarding local phase corrections, gate fidelity, and scalable implementations can be directly carried over.

The rationale for the above decomposition theorem is surprisingly simple. Let us re-examine the gate time evolution, which is governed by a grid vector that further decomposes into bond vectors $\mathbf{\Lambda} = \otimes_w \mathbf{\Lambda}_w$. Despite different bonds can share common dots, when viewed as diagonal matrices, all $\mathbf{\Lambda}_w$ commutes with each other. Hence the time-evolution decomposes automatically onto each bonds

$$\tilde{U}_{\text{ideal}} = \exp\left(i\tau \bigotimes_w \Lambda_w\right) = \prod_w \left(e^{i\tau \Lambda_w} \otimes I_{w\perp}\right), \quad (42)$$

where $I_{w\perp}$ is the identity on the orthogonal space of the bond w . The combined gate on the full grid is simply the product of gates on each bonds. The order of this product is irrelevant since all matrices commute.

As a result, we can view the MQCP gates as the product of multiple two-qubit controlled-phase gates with the same control qubit. As illustrated in Fig. 2(a) for a five-qubit example. The single quantum gate with a central qubit controlling multiple target qubits is equivalent to the product of multiple controlled-phase gates. Furthermore, for a general quantum dot array with a given connectivity, we can identify the achievable gate by decomposing the full array into multiple stellar-connected subgroups, each implementing a MQCP gate. The resulting gate may no longer be an MQCP gate. For example, consider the three-qubit ring in Fig. 2(b), the intrinsic gate is a product of three CPhase gates, and no particular qubit can stand out as the control qubit. The total

time evolution under such connectivity is equivalent to a product of those MQCP gates. This is demonstrated in Fig. 2(c) for a six-qubit array with two equivalent ways of decomposition.

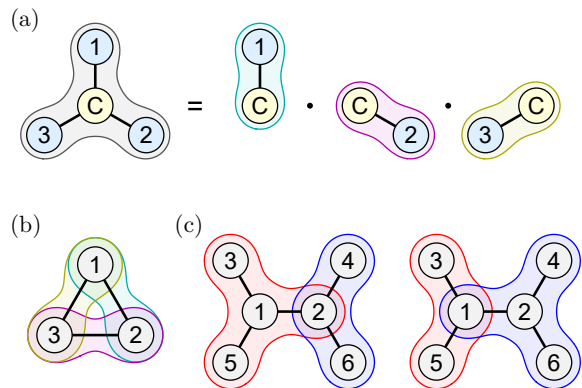


FIG. 2. Decomposition of intrinsic multi-qubit gates based on the dot connectivity. (a) The intrinsic gate for a four-qubit system in stellar configuration is an MQCP gate, which can be decomposed as the Kronecker product of three two-qubit CPhase gates. (b) The intrinsic gate of a three-qubit ring does not contain a control qubit, as the three qubits are totally symmetric to each other. (c) Two different ways of decomposing the same intrinsic gate for a six-qubit array as product of MQCP gates. The resulting local phase corrections are independent of particular choice of decomposition.

Proper local phase corrections are still required for a multi-qubit array to implement a product of MQCP gates. It is straightforward to show that the necessary phase corrections of a dot should be accumulate from each MQCP subgroups. This also explains the local phase identity $\phi_c = \sum_j \phi_j$ for a general MQCP gate, which can be decomposed into multiple two-qubit groups with $\phi_c = \phi_j$. While for more general arrays, there can have multiple viable ways of gate decomposition. Consider the example in Fig. 2(c), we have two different ways of decomposition into MQCP gates. At first sight, this ambiguity seems to give rise to uncertainties in local phase corrections. But it turns different ways of decompositions are just equivalent ways of understanding the same gate. For the Fig. 2(c) example, assuming that all bonds are homogeneous and satisfy the condition $(T-S)\tau = \pi/2$, we will have $\phi_1 = \phi_2 = 3\pi/2$ and $\phi_3 = \phi_4 = \phi_5 = \phi_6 = \pi/2$ for both decompositions. In general, the necessary local phase factors are found by

$$\phi_j = \sum_{j \in w} \tau(T_w - S_w), \quad (43)$$

that is, the necessary local phase correction for a dot is the summation of the accumulated phase of its connecting edges. Therefore, the local phase corrections are invariant to different ways of MQCP decomposition.

C. Estimation of the coherent error

We have hitherto replaced the actual rotating-frame map $\tilde{U}(\tau)$ with the ‘‘ideal’’ map \tilde{U}_{ideal} and investigated what can be achievable with the latter. However, the conditions for $\tilde{U}_{\text{ideal}} = G$ for a certain gate G do not imply that the same gate can be accurately implemented with $\tilde{U}(\tau)$. Difference between the actual and ideal maps is a coherent error in the gate implementation. In this section, we examine how much error is brought by making such approximation.

1. Fidelity bound

A implementation of quantum gate can be characterized with the average gate fidelity, defined by averaging the fidelity for output states over all input states. Here, we are concerned with estimating the fidelity loss by replacing \tilde{U} with \tilde{U}_{ideal} , both are unitary maps with the same dimensionality. The fidelity can be calculated by

$$F(\tilde{U}, \tilde{U}_{\text{ideal}}) = \frac{d + |\text{tr}(\tilde{U}^\dagger \tilde{U}_{\text{ideal}})|^2}{d(d+1)}, \quad (44)$$

where d is the dimension of the system [64]. A helpful simplification is brought by the fact that \tilde{U}_{ideal} is diagonal in the computational basis: we only need to focus on the diagonal elements of \tilde{U} for calculating the fidelity. Substituting in the diagonal elements in Eq. (10), we can compute the trace product by

$$\left| \text{tr}(\tilde{U}^\dagger \tilde{U}_{\text{ideal}}) \right| = \left| \sum_{n,m} r_{nm} e^{-i(\tau E'_m + \varphi_n)} \right|, \quad (45)$$

where

$$\varphi_n \equiv \tau(\delta E_n - \delta E_n^{(1)}) = \tau \sum_{k \geq 2} \delta E_n^{(k)}. \quad (46)$$

Using a combination of inequalities, we can estimate a upper bound for the gate infidelity $\text{InF} = 1 - F$ by

$$\text{InF} \leq \frac{4}{d+1} \sum_n (1 - r_{nn}) + \frac{1}{d+1} \sum_n \varphi_n^2. \quad (47)$$

We derive this inequality in the Appendix B. From this bound, we identify two contributing factors of coherent errors. One is the decreased overlap between the perturbed and unperturbed eigenstates $r_{nn} \lesssim 1$. The other is the residue phase φ_n accumulated in time from the higher-order energy corrections. The magnitudes of these terms can be estimated by carrying out second-order perturbation. The non-unit wave function overlap

$$1 - r_{nn} \simeq \sum_{m \neq n} \frac{|\langle n | H_{\text{ex}} | m \rangle|^2}{(E_n - E_m)^2} \quad (48)$$

contributes to the infidelity of second-order in the perturbative strength J/ε^Z . While the accumulated phase

$$\varphi_n \simeq \tau \sum_{m \neq n} \frac{|\langle n | H_{\text{ex}} | m \rangle|^2}{E_n - E_m} \quad (49)$$

appears quadratic in H_{ex} , the total evolution time τ is reversely proportional to J for typical quantum gates. Therefore the second term in Eq. (47) is also of second order in J/ε^Z .

The estimations in Eq. (48) and Eq. (49) make sense only when the eigenenergies of H_{qu} are non-degenerate. Indeed, as \tilde{U}_{ideal} is defined from the non-degenerate first-order perturbation, we expect the approximation $\tilde{U}(\tau) \approx \tilde{U}_{\text{ideal}}$ to fail if there is energy degeneracy. This is reflected in the diverging infidelity upper bound for the right-hand-side of Eq. (47). Although the degeneracy problem can be circumvented by imposing the additional condition $|E_m - E_n| > \|H_{\text{ex}}\|$ for all m, n , such requirement is impractical for system with a large number of quantum dots, in which the eigenenergies $\{E_n\}$ become densely packed. Therefore, a careful analysis accounting for accidental degeneracies is necessary.

A closer inspection of Eq. (48) and Eq. (49) reveals that it is not necessary to require $E_n \neq E_m$ for all $m \neq n$. In most cases, the numerator in the sum vanishes and does not contribute to gate error. The matrix element $\langle n | H_{\text{ex}} | m \rangle$ is non-zero only when the Hamming distance between m and n is less or equal to 2. In other words, for fixed $|n\rangle = |n_1, n_2, \dots, n_{N_Q}\rangle$, with spin component $n_j \in \{\uparrow, \downarrow\}$, we only need to consider the $|m\rangle$ states whose spin components differ from that of $|n\rangle$ in at most two locations. This is evident from the fact that H_{ex} is the Kronecker sum of four-dimensional matrices. Furthermore, for $\langle n | H_{\text{ex}} | m \rangle \neq 0$, the two dots corresponding to different spin components in $|n\rangle$ and $|m\rangle$ should be connected (with nonzero J coupling). As a result, we can reduce the infidelity bound into a summation of error contributions from each bond

$$\sum_n (1 - r_{nn}) \simeq \sum_w J_w^2 \sum_{n_w, m_w} \frac{|\langle n_w | \xi_w \rangle \langle \xi_w | m_w \rangle|^2}{(E_{n_w} - E_{m_w})^2} \quad (50)$$

$$\sum_n \varphi_n^2 \lesssim 2 \sum_w \tau^2 J_w^4 \sum_{n_w, m_w} \frac{|\langle n_w | \xi_w \rangle \langle \xi_w | m_w \rangle|^4}{(E_{n_w} - E_{m_w})^2}, \quad (51)$$

where $|n_w\rangle$ and $|m_w\rangle$ is the projection of $|n\rangle$ and $|m\rangle$ in the four-dimensional subspace of the bond w . For $w = \langle j, k \rangle$, the possible denominators in Eq. (50) and Eq. (51) are $\pm \frac{1}{2}(\varepsilon_j^Z + \varepsilon_k^Z)$ and $\frac{1}{2}(\varepsilon_j^Z \pm \varepsilon_k^Z)$. Therefore it is sufficient to require the Zeeman energies between neighboring dots to be non-degenerate, $|\varepsilon_j^Z - \varepsilon_k^Z| > J_{jk}$ —a much weaker condition than requiring all E_n to be non-degenerate. Physically, we can require the Zeeman energy splittings to differ across neighboring quantum dots by having significant g -factor variations or inhomogeneous magnetic field.

2. Reducing coherent error

It is possible to reduce the coherent error by applying *additional* local phase corrections to the values in Eq. (43) predicted by the first-order theory. This technique is already seen in two-qubit gates, where slightly different local phase corrections are applied for the two dots for improved fidelity [27].

We extend such idea to an intrinsic multi-qubit gate. Similar as the free phase map defined in Eq. (16), applying an extra set of local phase corrections to the multi-qubit gate \tilde{U} produces $\tilde{U}' = e^{i\delta\Phi}\tilde{U}$, with

$$\delta\Phi = \bigoplus_j (0, \delta\phi_j) \equiv K\delta\phi, \quad (52)$$

for additional phase shift $\delta\phi_j$ on dot j . For convenience, we introduce the vector $\delta\phi = (\phi_1, \phi_2, \dots, \phi_{N_Q})^T$ and the coefficient matrix K , which is only determined by N_Q and can be efficiently calculated. To compute the improved fidelity between \tilde{U}' and \tilde{U}_{ideal} , we only need to replace the vector of accumulated phases φ with the shifted values

$$\varphi \rightarrow \varphi' = \varphi - \delta\Phi = \varphi - K\delta\phi, \quad (53)$$

where the components of φ is given in Eq. (46). According to Eq. (47), the gate infidelity is contributed by the norm of the vector φ . Therefore, our goal is to find an optimal vector of extra phases $\delta\phi$ such that the norm of φ' is minimized. Now if K is invertible, it is easy to see that such optimal $\delta\phi = K^{-1}\varphi$. But K cannot be inverted for $n_Q \geq 2$ as it is a $2^{N_Q} \times N_Q$ dimensional. In such case, the optimal extra phase vector and correct phase vector is defined by

$$\delta\phi = K^+\varphi, \quad \varphi' = (I - K^+K)\varphi, \quad (54)$$

for the Moore-Penrose pseudoinverse $K^+ \equiv (K^T K)^{-1} K$ of K [65]. Combined with optimal values for the tunneling coefficients, the accumulated phases from second order energies correction $\delta E_n^{(2)}$ can be effectively suppressed.

To demonstrate the effect of extra phase corrections in practice. We explicitly consider the example of a MQCP gate on linear array of three-qubit (as “1-C-2”). Without loss of generality, we set $\tilde{s}_j = i \sin(\theta_j)$ and $\tilde{t}_i = e^{i\eta_j} \cos(\theta_j)$ for the tunneling coefficients for the two bonds $j = 1, 2$ connected to the center qubit, with exchange energies J_1 and J_2 . Applying applying the optimal local phase correction Eq. (54) to the φ vector specified by Eq. (49), we find $\varphi' \simeq \varphi_{\text{max}} \times (1, -1, -1, 1, -1, 1, 1, -1)^T$, with

$$\varphi_{\text{max}} = \tau \frac{J_1 J_2}{8\varepsilon_2^Z} \sin(2\theta_1) \sin(2\theta_2) \cos(\eta_1 - \eta_2). \quad (55)$$

The norm of φ' is much smaller than that of the uncorrected φ . In fact, from Eq. (55) we see that the second order error contribution can be fully reduced if the tunneling coefficients further satisfy conditions such as $\theta_j = k\pi/2$ or $\eta_1 - \eta_2 = (k + 1/2)\pi$ for $k \in \mathbb{Z}$.

D. Applications of multi-qubit gates

The rule of general gate decomposition allows us to conceive many intrinsic multi-qubit gates that can be useful for quantum information processing tasks. Here we consider three simple examples of their advantageous applications. Hopefully these discussion can inspire more sophisticated multi-qubit gates in the future.

1. Three-qubit logical Z-gate

Our first example is based on the three-qubit system. But instead of a linear geometry, this time we consider the case where all three qubits are all connected to each other, as shown in Fig. 2(b). From the gate decomposition law, the corresponding intrinsic gate can be decomposed as three controlled-phase gates, one for each connecting pair. Assuming that the bonds are homogeneous and that π -phase flips are applied, the combined gate becomes

$$G = (C_1 Z_2) \cdot (C_2 Z_3) \cdot (C_3 Z_1) \\ \cong \text{diag}(1, 1, 1, -1, 1, -1, -1, -1). \quad (56)$$

As a result, the $|000\rangle$, $|001\rangle$, $|010\rangle$ and $|100\rangle$ states are unaffected while $|011\rangle$, $|101\rangle$, $|110\rangle$ and $|111\rangle$ experience π -phase (sign) flips. In other words, the phase flips for G distinguishes the majorly $|0\rangle$ states with the majorly $|1\rangle$ states. Meanwhile, the non-entangling gate $X_1 X_2 X_3$ correctly interchanges the majorly $|0\rangle$ states with the majorly $|1\rangle$ states and also anticommutes with G . Based on this property, this three-qubit system can be considered as a error correction code for bit-flip errors, with the logical $|\bar{0}\rangle$ and logical $|\bar{1}\rangle$ encoded with states that are majorly $|0\rangle$ and majorly $|1\rangle$. The gate G in Eq. (56) becomes the logical \bar{Z} gate whereas $X_1 X_2 X_3$ becomes the logical \bar{X} . In comparison to G , we consider the simple product gate of $Z_1 Z_2 Z_3$, which flips the sign of the states $|001\rangle$, $|010\rangle$, $|100\rangle$ and $|111\rangle$. Both gates anticommute with $X_1 X_2 X_3$ and act the same on $|000\rangle$ and $|111\rangle$. But the $Z_1 Z_2 Z_3$ gate does not respect major voting like G , therefore it cannot serve as the logical \bar{Z} for our code.

2. Simultaneous parity checks

The ability to perform parity measurements on different qubits is a fundamental requirement for many quantum error correction codes [66]. It turns out that the MQCP gates are particularly suitable for such parity measurement tasks. We demonstrate some explicit examples of MQCP as parity checkers in Fig. 3.

Let us first consider the circuit in Fig. 3(a) for a three-qubit system. This circuit can be broken down into three steps: (1) preparing the middle qubit in the $|+\rangle$ state; (2) applying a $CZ_1 Z_2$ gate with the middle qubit as control; (3) measuring the control qubit in the $|+\rangle$

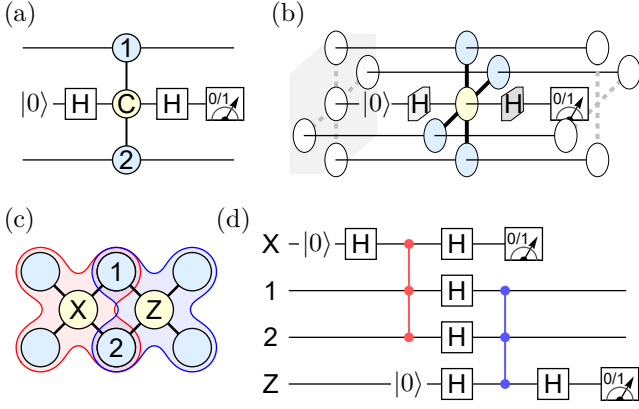


FIG. 3. Example demonstrations of simultaneous parity checks through MQCP gates. (a) The quantum circuit to perform parity check of the Z_1Z_2 operator. The circuit can also be slightly modified to perform parity check of the X_1X_2 operator. (b) A two-dimension parity check circuit that simultaneously check the parity of the four neighboring qubits by application of the $CZ_1Z_2Z_3Z_4$ gate and measurement of the controlled qubit. (c) A basic unit cell of the surface code that involves data qubits with X and Z parity check maps. Both of these maps can be efficiently carried out using MQCP gates. (d) The circuit diagram of the surface code stabilizing cycle for the shared data qubit 1 and 2. The red and blue vertical lines joining three circuit wires are an application of CZ_1Z_2 gates, with the control qubits X and Z as in (c).

basis. It can be directly worked out that the measurement outcome will project the other two qubits into ± 1 eigen-spaces of the Z_1Z_2 operator. Hence this circuit is tantamount to a simultaneous parity check of the upper and lower qubits. This circuit can also be adapted to measure the parity of the X_1X_2 operator by appending extra Hadamard gates H_1H_2 after the CZ_1Z_2 gate. In Fig. 3(b), we extend the tree-qubit parity measurement circuit to a two-dimensional array. The measurement qubit now serves as the control qubit in the $CZ_1Z_2Z_3Z_4$ gate. One can verify that the circuit measures the parity of the joint Z - or X - operator of the surrounding target qubits. The equivalent parity check circuit can be certainly build using two-qubit gates. Compared with the equivalent circuit with four CNOT gates applied at different time step [21], the parity check circuits in Fig. 3(b) only require one multi-qubit gate and the parity of the target qubits are measured simultaneously.

The advantages of MQCP gates as simultaneous parity checks are obvious for large scale codes with many parity checks. In particular, the MQCP parity checks can be used as an basic element for the constructing surface code. Following an example in Ref. [21], we consider a “unit cell” of surface code with one X and one Z parity check operators, as illustrated in Fig. 3(c). We implement the X and Z parity checks with the red and blue colored MQCP gates repetitively. These two gates are separated by single-qubit Hadamard gates for transforming the $|0/1\rangle$ basis with the $|\pm\rangle$ basis. Fig. 3(d) is

a detailed breakdown of such simultaneous parity check for qubit 1 and 2, where the red and blue vertical lines are corresponding MQCP gates. Following this circuit, one can verify that the final state for qubit 1 and 2 is stabilized to a simultaneous eigenstate of the Z_1Z_2 and X_1X_2 operator. Compared with equivalent circuit using two-qubit gates, the MQCP gate approach requires significantly less entangling gates, and is capable of measuring the parity of all qubits simultaneously. This could dramatically reduce the error rate associated with the parity measurement process.

3. Fast order reversal

Some quantum computing tasks require reversing the order of a set of states—notably, this step is involved in quantum Fourier transform [66]. Assuming that a multi-qubit state is stored in a linear array of N qubits, the task of order reversal is to “flip” the array such that the basis state $|\mathbf{n}\rangle$ is swapped with its reversed state $|\overleftarrow{\mathbf{n}}\rangle$,

$$|\mathbf{n}\rangle = |n_1, n_2, \dots, n_N\rangle \leftrightarrow |n_N, \dots, n_2, n_1\rangle \equiv |\overleftarrow{\mathbf{n}}\rangle, \quad (57)$$

e.g., $|0011\rangle \leftrightarrow |1100\rangle$. The map should be linear such that any quantum entanglement is preserved.

The quantum circuit for reversing the array typically breaks down into multiple application of swap gates, which is only allowed for near-neighbors due to restriction in connectivity. In general, flipping an N -qubit array requires $N(N-1)/2$ near-neighbor swaps, with each swap made up of three CNOT gate (or CZ combined with single-qubit Hadamard gates). Although some swaps can be simultaneously performed, the task still requires $O(N^2)$ steps to accomplish. However, such array reversal task can be achieved with only N applications of the intrinsic multi-qubit gate L with π -phase flips on all bonds. Such gate can be decomposed as the product

$$L = (C_1Z_2) \cdot (C_2Z_3) \cdots (C_{N-1}Z_N). \quad (58)$$

Consider the following gate sequence that interleaves the L gate with single-qubit Hadamard gates $H = H_1 \otimes H_2 \otimes \cdots \otimes H_N$,

$$R = HLHL \cdots HLGH = H(LH)^N. \quad (59)$$

Using the stabilizer group formalism [67], we can show that R differs from the order reversal map only by single-qubit sign flips depending on the parity of the states,

$$R : |\mathbf{n}\rangle \leftrightarrow p(\mathbf{n}) \times |\overleftarrow{\mathbf{n}}\rangle, \quad (60)$$

where the parity function $p(\mathbf{n}) = \pm 1$ depends on the number of consecutive 1 in string \mathbf{n} , with even and odd number of consecutive 1 producing $p = +1$ and $p = -1$. For example, the even parity strings “00010” and “01110” contain 0 and 2 occurrence(s) of consecutive 1, compared with the odd-parity strings “00110” and “01111” with 1 and 3 occurrence(s). The matrix representation of R is

plotted in Fig. 4 for the examples of a linear array of 3, 4 and 5 qubits for demonstration. These extra sign flips can further corrected in the software level following the above specified rule. As a result, application of the multi-qubit gate accelerate the order reversal task to $O(N)$ time steps, compared with the equivalent circuit of two-qubit gates taking $O(N^2)$ steps.

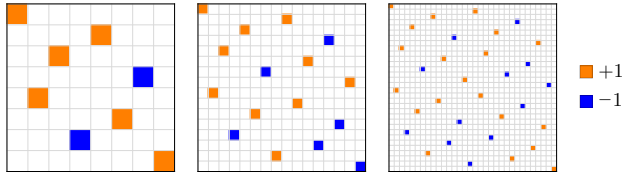


FIG. 4. Matrix representations of the array reversal map R in Eq. (60) for $n = 3, 4, 5$ (from left to right). The matrices differ from the corresponding array reversal maps only by negative signs for some states.

IV. SCALABLE IMPLEMENTATIONS

A. The problem of bond inhomogeneity

For MQCP gates, the dynamics rule Eq. (38) specifies the condition that must be met by the connecting bonds in order to implement the target gate. Examining the dynamics rule, for example, of the CZ_1Z_2 gate,

$$\begin{cases} \frac{\tau}{2\pi}(T_1 - S_1) = k_1 + \frac{1}{2} \\ \frac{\tau}{2\pi}(T_2 - S_2) = k_2 + \frac{1}{2} \end{cases}, \quad k_1, k_2 \in \mathbb{Z}. \quad (61)$$

One way to think of the gate dynamics is to examine the “phase space” picture. As as illustrated in Fig. 5, the target gate is specified by a lattice of half-integer points. Time evolution traces out a parametric path of τ , which is a straight line with the tangent vector $\mathbf{v} \propto (T_1 - S_1, T_2 - S_2)$. The goal for time evolution is to bump into one of the lattice points. In the ideal case, $T_1 - S_1 = T_2 - S_2$ and the path would directly heads towards the first lattice point at $(1/2, 1/2)$. This corresponds to the theoretically minimal evolution time of $\tau = \pi/(T - S)$, which is the same as that of the CZ gate in despite of more target qubits. In reality, due to structural defects and imperfections, it is unlikely to have completely identical interdot couplings. The difference in the two bonds results in unwanted error in implementing the target gate.

As the target can be any lattice point, it is still possible for the evolution path to bump into some lattice point even if the bonds are inhomogeneous. However, for perfectly attaining a lattice point, the ratio for velocity components must be rational. For irrational velocity ratios, the evolution path can never come across a lattice point, as illustrated with the thin blue line in Fig. 5(a).

Instead, the evolution path can get arbitrarily close to a lattice point given sufficiently long time. To demonstrate this property, we define the “reduced” phase space as the first lattice indicated by the shaded area in Fig. 5(a). Due to the periodic nature of the target gate, we can fold the full evolution path into the reduced phase space. The results are illustrated in Fig. 5(b) and Fig. 5(c) for the rational and irrational path. For the rational path, the trajectory attains the target point after finite cycles. For the irrational path, the trajectory will densely covers the reduced phase space given sufficient time.

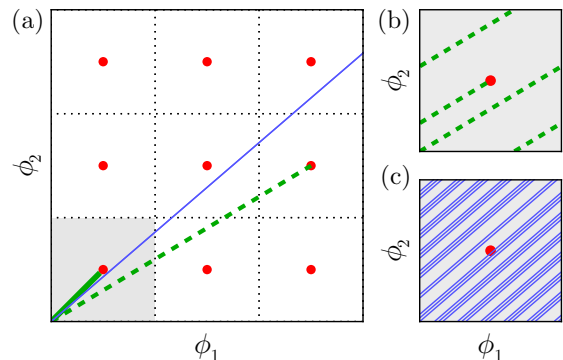


FIG. 5. (a) DC evolution path in the (extended) phase space. The red lattice points represent the target gate and straight lines represent different evolution paths: the ideal case with identical bonds (thick green line), bonds with mutually rational strengths (dashed green line) and bonds with mutually irrational strengths (thin blue line). (b) and (c), the reduced phase space time evolution for the rational and irrational bonds.

Although the above discussion is based on the CZ_1Z_2 gate, similar conclusions hold for a general $(N + 1)$ -qubit MQCP gate. One only need to replace the two-dimensional picture with a similar N -dimensional version, and the “velocity” vector by $\mathbf{v} = (T_1 - S_1, T_2 - S_2, \dots, T_N - S_N)$, with different coupling strengths corresponding to different velocity complements. Despite that the target point can be eventually approached, the time would take too long for large systems. In fact, the worst-case time required to achieve gate infidelity ϵ scales super-exponentially with N ,

$$\tau \propto \Gamma\left(\frac{N}{2}\right) \left(\frac{8}{\epsilon\pi N}\right)^{(N-1)/2}, \quad (62)$$

where $\Gamma(\cdot)$ is the gamma function [68]. It is very likely the during these time, the qubit will decohere beyond recognition! Although it is possible to fine-tune the bond strength for small systems, the issue of inhomogeneity poses a major challenge when the size of the qubit chip scales up. For scalable multi-qubit gates, one must find an efficient way to overcome the bond inhomogeneity.

We propose a control scheme that can effectively eliminate the bond inhomogeneity issue. The grand idea is to “steer an artificial path” in the phase space with external pulses. Inspired by the dynamical decoupling proto-

col [52], we refer such protocol as dynamical calibration, in the sense that the bond strength are calibrated dynamically with pulses. The scheme scales well with the number of qubits, as only fast single-qubit pulses are required. In the followings, we will first explore this ideal with some examples, and then present a general theory of dynamical calibration.

B. Dynamical calibration: examples

Till now, we have only considered time evolutions with time-independent control, i.e., the exchange coupling is turned on and stays constant during the full evolution. This is often termed as DC gates [27]. So-far we have approximated the rotating-frame map at time τ with

$$\tilde{U}_T = e^{i\tau H_0} e^{-i\tau H} \simeq e^{i\tau \Lambda}, \quad (63)$$

where we set time origin at 0 for brevity, $H = H_0 + H_{\text{ex}}$ and the approximation is achieved in the perturbative limit $\|H_0\| \gg \|H_{\text{ex}}\|$ and does not depend on τ .

Going beyond the simple DC-control scheme, let us consider applying a bit-flip pulse X_j to the j -th qubit at time $\tau_1 < \tau$. Assuming the pulse width to be much shorter than the time duration for achieving the full multi-qubit gate, we can apply a similar perturbative treatment to calculate the resulting quantum gate

$$\begin{aligned} \tilde{U}_{X_j} &= e^{i\tau H_0} e^{-i(\tau-\tau_1)H} X_j e^{-i\tau_1 H} \\ &\simeq X_j e^{-i\tau_1 \varepsilon_j^Z \sigma_j^Z} \exp[i(\tau - \tau_1) X_j \Lambda X_j + i\tau_1 \Lambda], \end{aligned} \quad (64)$$

where we have use the fact that both $X_j H_0 X_j$ and $X_j \Lambda X_j$ are diagonal to commute and combine matrix exponentials. The first and second terms in Eq. (64) are extra bit-flip and local phase shift for the j th qubit, while the last term is responsible for entangling different qubits. As argued earlier, local phase shifts can be compensated in the software level. The extra bit-flip can be combined with upcoming gates or recovered by applying another X_j pulse at τ . In the later case, we have

$$\begin{aligned} \tilde{U}_{X_j X_j} &= e^{i\tau H_0} X_j e^{-i\tau_2 H} X_j e^{-i\tau_1 H} \\ &\simeq e^{i\tau_2 \varepsilon_j^Z \sigma_j^Z} \exp[i(\tau_2 X_j \Lambda X_j + \tau_1 \Lambda)], \end{aligned} \quad (65)$$

which produces a different local phase without the extra bit-flip. The entangling part, same in both cases, can be seen as time evolution under the normal grid vector Λ , followed by the conjugated grid vector $X_j \Lambda X_j$ for the period of τ_1 and τ_2 respectively.

Using Eq. (13), we can see that the X_j conjugation is only relevant to the bonds containing dot j ,

$$X_j \Lambda X_j = \sum_{j \in w} J_w \text{diag}(|\xi'_w\rangle \langle \xi'_w| \otimes I_w^\perp) + \sum_{j \notin w'} \Lambda_{w'}, \quad (66)$$

where $|\xi'_w\rangle \equiv X_j |\xi_w\rangle$ is the flipped entangled state containing dot j . Effectively, the X_j pulse swap the

spin-conserved and spin-flipped tunneling strength $T_w = J|t_w|^2$ and $S_w = J_w|s_w|^2$. For multi-control gates, exchanging T and S tunneling channel of a bond results in a reversal of its effective velocity component. This offers a control possibility where we can design an customize path in the phase space to the target gate by applying single qubit pulses at appropriate intervals.

To better demonstrate this idea, we again consider the three qubit CZZ gate, with bonds connecting the control qubit c to the target qubit j ($j = 1, 2$), on which live the entangled states

$$|\xi_{cj}\rangle = \tilde{s} |\uparrow\uparrow\rangle_{cj} - \tilde{t} |\uparrow\downarrow\rangle_{cj} + \tilde{t}^* |\downarrow\uparrow\rangle_{cj} + \tilde{s}^* |\downarrow\downarrow\rangle_{cj}, \quad (67)$$

where we omit the normalization factor $1/\sqrt{2}$ and the subscripts for t and s for brevity. Applying bitflip to the target or control qubit results in,

$$\begin{aligned} X_j |\xi_{cj}\rangle &= -\tilde{t} |\uparrow\uparrow\rangle_{cj} + \tilde{s} |\uparrow\downarrow\rangle_{cj} + \tilde{s}^* |\downarrow\uparrow\rangle_{cj} + \tilde{t} |\downarrow\downarrow\rangle_{cj}, \\ X_c |\xi_{cj}\rangle &= \tilde{t}^* |\uparrow\uparrow\rangle_{cj} + \tilde{s}^* |\uparrow\downarrow\rangle_{cj} + \tilde{s} |\downarrow\uparrow\rangle_{cj} - \tilde{t} |\downarrow\downarrow\rangle_{cj}. \end{aligned} \quad (68)$$

In both cases, the relevant spin-conserved and spin-flipped tunneling strengths are exchanged $T \leftrightarrow S$. In terms of the phase space velocity $\mathbf{v} = (T_1 - S_1, T_2 - S_2)$, the X_j pulse flips the velocity component $v_j \rightarrow -v_j$ while the X_c pulse flips *both* velocity components. Supposing $v_1 > v_2 > 0$, the simplest scheme to overcome bond inhomogeneity is to apply a X_1 pulse at time instant $\tau_1 = \frac{1}{4}(v_1^{-1} + v_2^{-1})$, as illustrated by the path in Fig. 6(a). The total gate time $\tau = 1/2v_2$ is determined by the weaker bond of the two. Alternatively, one can apply two X_1 pulses symmetrically to cancel out the effect of the remaining X gate, show by the path in Fig. 6(b). One step further, one can apply pulses to all three qubits in the order of X_1 , X_2 and X_c , separated by time duration τ_1 , τ_2 and τ_3 respectively. The corresponding rotating-frame evolution can be calculated to be

$$\begin{aligned} \tilde{U}_{X_c X_2 X_1} &= e^{i\tau H_0} e^{-i\tau_4 H} X_c e^{-i\tau_3 H} X_2 e^{-i\tau_2 H} X_1 e^{-i\tau_1 H} \\ &\simeq X_c X_2 X_1 e^{-i\phi'_c \sigma_c^Z} e^{-i\phi'_2 \sigma_2^Z} e^{-i\phi'_1 \sigma_1^Z} e^{i \sum_{k=1}^4 \tau_k \Lambda_k}. \end{aligned} \quad (69)$$

Apart from single-qubit bit-flips $X_c X_2 X_1$, the pulses also induce local phase shifts $\phi'_c = (\tau_1 + \tau_2 + \tau_3) \varepsilon_c^Z$, $\phi'_2 = (\tau_1 + \tau_2) \varepsilon_2^Z$ and $\phi'_1 = \tau_1 \varepsilon_1^Z$, which are correctable by virtual- Z gates. The entangling part is determined by a four-step time evolution, under the effective grid vectors $\Lambda_1 = \Lambda$, $\Lambda_2 = X_1 \Lambda X_1$, $\Lambda_3 = X_2 X_1 \Lambda X_1 X_2$, and $\Lambda_4 = X_c X_2 X_1 \Lambda X_1 X_2 X_c$ for the time duration of τ_1, τ_2, τ_3 , and $\tau_4 \equiv \tau - (\tau_1 + \tau_2 + \tau_3)$ respectively. The phase space path is illustrated in Fig. 6(c).

Compared with a single X_1 pulse, one key advantage of pulsing all three qubits is its potential to be combined with dynamical decoupling, where all three qubits can be protected by decoupling pulses while performing the gate. Specifically, let us consider applying the $XYXY$ sequence to each of the qubits. For the system-environment coupling Hamiltonian of H_{SB} , the net effect of the se-

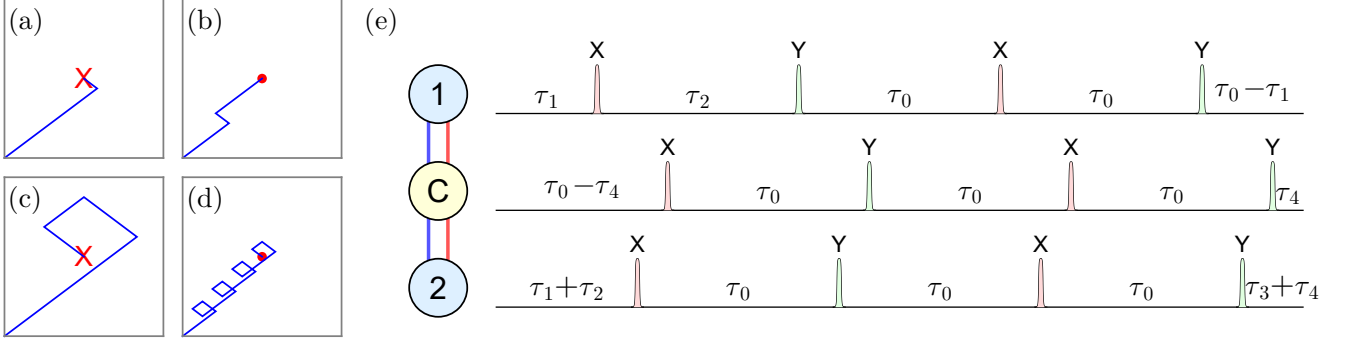


FIG. 6. (a-d): The phase-space path with (a) a single X pulse, (b) a pair of X pulses, (c) three X pulses on all qubits, (d) the X - Y - X - Y dynamical decoupling sequence applied to all qubits. In the figure, the target gate is the red point in the center of the rectangle, while a cross-mark represents that the sequence results in extra X gates to be accounted later. (e): The temporal decomposition of the relevant single qubit pulses in the dynamical decoupling sequence of (d). The dot array is shown in the left inset, followed by X and Y pulses on relevant dots with different separation in time.

quence on a single qubit is

$$\begin{aligned} U_{\text{DD}} &= Y e^{-i\tau_0 H_{\text{SB}}} X e^{-i\tau_0 H_{\text{SB}}} Y e^{-i\tau_0 H_{\text{SB}}} X e^{-i\tau_0 H_{\text{SB}}} \\ &= e^{-i\tau_0 (Y H_{\text{SB}} Y + Z H_{\text{SB}} Z + X H_{\text{SB}} X + H_{\text{SB}})} + O(H_{\text{SB}})^2, \end{aligned} \quad (70)$$

The Pauli group twirling results in identity on the system part, hence the pulse sequence can suppress environmental coupling to the first order. Similar to the X -pulse, a Y -pulse acts on the entangled state by

$$\begin{aligned} Y_j |\xi_{cj}\rangle &= -i\tilde{t}^* |\uparrow\uparrow\rangle_{cj} + i\tilde{s}^* |\uparrow\downarrow\rangle_{cj} - i\tilde{s} |\downarrow\uparrow\rangle_{cj} - i\tilde{t} |\downarrow\downarrow\rangle_{cj}, \\ Y_c |\xi_{cj}\rangle &= i\tilde{t} |\uparrow\uparrow\rangle_{cj} - i\tilde{s} |\uparrow\downarrow\rangle_{cj} + i\tilde{s}^* |\downarrow\uparrow\rangle_{cj} + i\tilde{t}^* |\downarrow\downarrow\rangle_{cj}. \end{aligned} \quad (71)$$

which also exchanges the T and S tunneling strengths of a particular bond. Based on this similarity between X and Y pulses, we can devise a dynamical calibration scheme that involves interleaved X and Y pulses. The pulsing choice and timing breakdown is illustrated in Fig. 6(e). This dynamical calibration seems like a trivial repetition of the four-staged evolution with X_1, X_2 and X_3 pulses in the phase space, see Fig. 6(d), but the reduced pulse sequence for each qubit is now a dynamical decoupling sequence. While the qubits are decoupled from the environment, they still remain coherently coupled to each other so that a MQCP gate can be performed. Hence we see that our dynamical calibration scheme not only is capable of mitigating the inhomogeneity error, but also enhances the overall qubit quality.

C. Dynamical calibration: general theory

We now present a general theory for the pulsed evolution in the presence of bond inhomogeneity. For an array of quantum dots with given connection, the intrinsic gate can be decomposed into the product of MQCP gates. The dynamics rule of the gate reduces to the time evolution in a high-dimensional phase spaces according

the equation

$$\tau \Delta = \phi = -\frac{1}{2} \boldsymbol{\theta} \pmod{\pi}, \quad (72)$$

where $\Delta = (\Delta_1, \Delta_2, \dots)$ is the vector of the *effective* strength for all the connecting bonds for $\Delta_w = T_w - S_w$, and $\boldsymbol{\theta} = (\theta_1, \theta_2, \dots)$ is the vector of target phase factors. The π -modulus implies that the target gate is represented by a high-dimensional lattice of target points. To implement simultaneous multi-qubit controlled- Z gates, all components of $\boldsymbol{\theta}$ are equal to π and it is desirable that the effective strength Δ_w for all the participating bonds are all equal. In practice, the bond strength may differ from ideal values, resulting in unwanted errors in gate implementations.

We seek to dynamically calibrate the bond strengths into a uniform value. This is done by keeping the dots coupled while inserting single-qubit pulses during the evolution. In general, we can write the qubit-frame time evolution operator for the pulsed evolution as

$$\begin{aligned} \tilde{U}_P &= e^{i\tau H_0} \cdot e^{-i\tau_N H} P_N e^{-i\tau_{N-1} H} P_{N-1} \\ &\quad \dots P_2 e^{-i\tau_1 H} P_1 e^{-i\tau_0 H}, \end{aligned} \quad (73)$$

where the pulse P_n is applied at time instance $\tau_0 + \tau_1 + \dots + \tau_n$ to some vertex point, within the total duration $\tau = \tau_0 + \tau_1 + \dots + \tau_N$. The reverse rotation $e^{i\tau H_0}$ in Eq. (73) transforms the lab-frame map to the qubit-frame. The P_n gates are chosen from the Pauli group and they compose into $P_N P_{N-1} \dots P_1 = Q$. To proceed, we introduce a set of auxiliary gates $\{Q_n\}$ according to $Q_n = P_n P_{n-1} \dots P_1$, with $Q_0 = I$ and $Q_N = Q$. The time evolution can be rewritten as

$$\begin{aligned} \tilde{U}_P &= e^{i\tau H_0} Q \prod_{n=0}^N Q_n^\dagger e^{-i\tau_n H} Q_n \\ &\simeq e^{i\tau H_0} Q \prod_{n=0}^N e^{-i\tau_n Q_n^\dagger H_0 Q_n} e^{i\tau_n Q_n^\dagger \Lambda Q_n}, \end{aligned} \quad (74)$$

where we have invoked the approximation Eq. (63) for each time fragment in Eq. (74). Since H_0 involves only Pauli-Z operators $\{\sigma_j^Z\}$, conjugation of H_0 by Q_n only selectively flips the signs for the σ_j^Z operators and the resulting matrix is still diagonal in the computational basis. Hence we can commute and combine terms in Eq. (74) and further obtain

$$\tilde{U}_P \simeq Q \cdot \bigotimes_j \exp(i\phi'_j \sigma_j^Z) \cdot \prod_{n=0}^N \exp(i\tau_n \Lambda^{(n)}). \quad (75)$$

The time evolution now comprises of three parts. First, an extra Pauli gate Q is introduced by the applied pulses. It can be combined with latter gates in the circuit. Alternatively, we can simply choose a pulse sequence composing into $Q = I$. The second part in Eq. (75) is a set of local phase shifts induced by the X_j and Y_j conjugations with σ_j^Z . Assuming $Q_n = \bigotimes_j Q_{nj}$ with $Q_{kj} \in \{I, X, Y, Z\}$ for the j th qubit in the array. For a given pulse scheme, the additional phases is explicitly determined by

$$\phi'_j = \sum_{n=0}^N \frac{1}{2} [\text{sig}(Q_{Nj}) - \text{sig}(Q_{nj})] \varepsilon_j^Z, \quad (76)$$

where $\text{sig}(I) = \text{sig}(Z) = 1$ and $\text{sig}(X) = \text{sig}(Y) = -1$. The extra local phase shifts can be easily corrected with virtual-Z gates and we may ignore them. The third part in Eq. (75) describes the entangling dynamics of the array, which is a simple product of $N + 1$ time-independent stages. Each stage is generated by a Pauli-conjugated grid vector $\Lambda^{(n)} \equiv Q_n^\dagger \Lambda Q_n$ that can be decomposed as the Kronecker sum

$$\Lambda^{(n)} = \bigoplus_{w=(j,k)} Q_{nj}^\dagger Q_{nk}^\dagger \Lambda_w Q_{nj} Q_{nk}, \quad (77)$$

By expressing each bond vector as the diagonal matrix $\Lambda_w \hat{=} \text{diag}(S_w, T_w, T_w, S_w)$, one can directly verify that X or Y conjugations on either dot exchange the T_w and S_w tunneling coefficients, while Λ_w is invariant under Z conjugations. Applying X or Y conjugation to both j and k exchanges the tunneling coefficients twice and leaves the bond vector in its original state. For example, $X_j \Lambda_w X_j = Z_j Y_k \Lambda_w Z_j Y_k \hat{=} \text{diag}(T_w, S_w, S_w, T_w)$ and $X_j Y_k \Lambda_w X_j Y_k = \Lambda_w$. The exchange of tunneling coefficients effectively results in a reversal of velocity component for bond w , $\Delta_w \rightarrow -\Delta_w$. For the entire array of dots, an X or Y gate applied to one vertices point will simultaneously reverse the velocities for all the bonds connected to that dot. Combined with the geometry of the array, each Q_n specifies the signs for all the bond velocity components. The $\Lambda^{(n)}$ at different stages of evolution are just different combinations of bond velocity components to be integrated with evolution time. This provide a method to dynamically calibrating the bond strength by properly choosing the time and locations of applied pulses.

Proper arrangement of the control pulses is the central to dynamic calibration. The arrangement of pulses is further determined by the connectivity of the array. If the array is loopless, i.e., the connecting bonds do not form a loop, such as the ones in Fig. 2, it is apparently possible to reverse each bond independently. A pulse scheme to calibrate all bonds can be easily constructed. If the array topology involves loops, it is impossible to reverse all bonds independently. There, one must adopt combinations of different bond reversal schemes to find consistent solutions for the pulse locations and intervals.

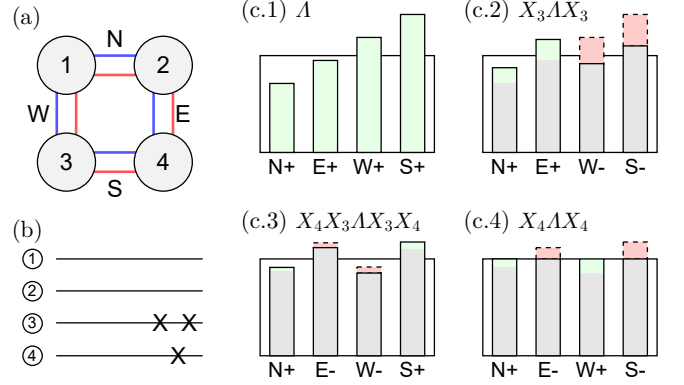


FIG. 7. A minimal dynamic calibration scheme for a rectangle grid. (a) The connectivity structure of the grid, composing of dot 1-4 and bonds N, E, W and S with inhomogeneous (increasing) bond strength. (b) The simplified circuit diagram for the calibration scheme, featuring a total of three X pulses on dot 3 and dot 4. (c.1-4) Break down of the phase factors accumulated in each stage of evolution for the four bonds. The green and red colored bars represent increment and decrement of the accumulated phase in a particular stage, while grey bars are phases accumulated in the previous stage. The effective grid vector for each stage is labeled above the bar charts.

To demonstrate dynamical calibration under sophisticated connectivity, we consider the rectangular grid example shown in Fig. 7(a). The dots are connected with four inhomogeneous bonds labeled by ‘N’, ‘E’, ‘W’ and ‘S’. Without loss of generality, we assume $\Delta_N < \Delta_E < \Delta_W < \Delta_S$. The accumulated phases can be dynamically calibrated to reach identical values using the pulses schematically plotted in Fig. 7(b). The time evolution is split into the following four-stage process. At stage 1, the array evolves naturally under the grid vector Λ . An X pulse is applied to qubit 3 before stage 2. This transforms the grid vector into $X_3 \Lambda X_3$ and reverses the velocity components of bond ‘W’ and ‘S’. Hence the accumulated phase for bond ‘W’ and ‘S’ seems a decrease while the phases increase for ‘N’ and ‘E’. This is then followed by an X_4 pulse, transforming the grid vector for the third stage into $X_3 X_4 \Lambda X_3 X_4$ and reversing the velocities for bond ‘E’ and ‘W’. An X_4 pulse is then applied and transforms the grid vector for the final stage as $X_4 \Lambda X_4$. The time-integrated phases for the four stages

are shown in the bar charts Fig. 7(c.1-4). Assuming that the target phase is ϕ for all the bonds, the time durations τ_0 to τ_3 of the four stages can be solve by

$$\begin{pmatrix} 1 & 1 & 1 & 1 \\ 1 & 1 & -1 & -1 \\ 1 & -1 & -1 & 1 \\ 1 & -1 & 1 & -1 \end{pmatrix} \begin{pmatrix} \tau_0 \\ \tau_1 \\ \tau_2 \\ \tau_3 \end{pmatrix} = \begin{pmatrix} \phi/\Delta_N \\ \phi/\Delta_E \\ \phi/\Delta_W \\ \phi/\Delta_S \end{pmatrix} \pmod{\pi}. \quad (78)$$

We see that the column of the sign matrix corresponds to the signs of the connecting bond ‘N’, ‘E’, ‘W’ and ‘S’ of a particular stage.

In order for the dynamical calibration protocol to work in the most general cases, we wish to find an appropriate pulse scheme to calibrate the bond strengths for any quantum dot array with arbitrary connectivity. Here we prove that there is always an appropriate pulse scheme for the fully connected array. Note that this automatically indicates that an array with arbitrary connection can be calibrated as well, as the later is only a subset of the former. It suffices to only consider assigning X gates to the fully connected dot array. A particular assignment of X gates, flips the bond velocities $(\Delta_1, \Delta_2, \Delta_3, \dots)$ according to an assignment vector, e.g, $\mathbf{a}_k = (+1, -1, +1, \dots)^T$ with $|\mathbf{a}_k| = n(n-1)/2 \equiv N_b$ for a fully connected array of n dots. There are 2^n distinctive ways of assigning X gates to the vertices, but different assignments can lead to same bond reversal scheme. We assume that there are at least N_a linearly independent assignment vectors. The pulses intervals are solved in an equation similar to Eq. (78),

$$\begin{pmatrix} | & | & \cdots & | \\ \mathbf{a}_1 & \mathbf{a}_2 & \cdots & \mathbf{a}_{N_a} \\ | & | & \cdots & | \end{pmatrix} \begin{pmatrix} \tau_1 \\ \tau_2 \\ \vdots \\ \tau_{N_a} \end{pmatrix} = \begin{pmatrix} \tilde{\phi}_1 \\ \tilde{\phi}_2 \\ \vdots \\ \tilde{\phi}_{N_b} \end{pmatrix} \pmod{\pi}, \quad (79)$$

where $\tilde{\phi}_n \equiv \phi_n/\Delta_n$ is the effective bond phase to be accumulated. If $N_a \geq N_b$, i.e., there are same or more linearly independent assignment schemes than the number of bonds, the pulse intervals can be found by solving this under-determined set of equations. Moreover, the π modulus guarantees that the pulse intervals can always be non-negative $\tau_n \geq 0$. It is straightforward to check that indeed $N_a = 4 > N_b = 3$ for a fully connected triple-dot array. We can prove $N_a > N_b$ for arbitrary array using mathematical induction. Assuming this inequality holds for an n -dot array, we consider a similar condition to Eq. (79) for an array with $n+1$ dots. By adding a dot to the array, n additional bonds are created. We collect the signs for these extra bonds by the $\{\mathbf{b}_k\}$ vectors for the k th assignment of X gates. We now have N_a assignments with the additional dot unchanged and N_a assignments with an X gate applied to the additional dot. These two states should have opposite signs for the extra bonds. In other words, we can write down

the following matrix for the assignment vectors,

$$\left(\begin{array}{cccc|cccc} \mathbf{a}_1 & \mathbf{a}_2 & \cdots & \mathbf{a}_{N_a} & \mathbf{a}_1 & \mathbf{a}_2 & \cdots & \mathbf{a}_{N_a} \\ \mathbf{b}_1 & \mathbf{b}_2 & \cdots & \mathbf{b}_{N_a} & -\mathbf{b}_1 & -\mathbf{b}_2 & \cdots & -\mathbf{b}_{N_a} \end{array} \right). \quad (80)$$

Since the column vectors $\{\mathbf{a}_k\}$ are linearly independent by assumption, the extended column vectors $\{(\mathbf{a}_k, \pm\mathbf{b}_k)\}$ must also be linearly independent. Hence when n is increased by one,

$$N_a^{(n+1)} \geq 2N_a^{(n)} = n(n-1) \geq \frac{(n+1)n}{2} = N_b^{(n+1)} \quad (81)$$

for $n \geq 3$. This proves our induction hypothesis.

D. Tunable connectivity with SOI

The typical methods to switch on-and-off the interaction between neighboring spins require either biasing the dot chemical potentials or lowering the tunneling barrier between neighboring dots. In essence, these methods can be viewed as the modulation of the exchange coupling energy J . This approach works well for two qubit systems, as verified by recent progresses reporting high fidelity figures. However, there are two problems that can hinder the wider application of such approach. First, the interdot coupling cannot be completely cut-off. Experimentally, J is modulated over several order of magnitudes to distinguish the ‘on’ and ‘off’ state. The residue coupling at ‘off’ state will result in errors that accumulate through the circuit. Second, such method does not scale well in terms of the control resources. Modulating the voltage of one particular gate electrode necessarily impact the the exchange coupling of all surrounding dots. As a result, the voltages on many gate electrodes must be adjusted simultaneously. The knowledge of how all the gates should synchronously change is obtained through prior calibration stage. One can imagine the tremendous efforts required to accurately calibrate and control the interdot coupling in a quantum chip with millions of qubits. A viable solution to this issue is to introduce tunable couplers between dots, such as superconducting Josephson junctions or transmon qubits [69]. Here we propose a whole new approach to control interdot coupling based on the theory developed in this work.

One key indigent in our theory is the inclusion of SOI. This effect result in an additional spin-flipping channeling when tunneling among dots. However, as suggested by Eq. (38), these two channels act destructively to constitute an effective bond strength

$$\Delta_w = T_w - S_w = \frac{1}{2}J_w (|\tilde{t}_w|^2 - |\tilde{s}_w|^2). \quad (82)$$

The typical methods to control inter-qubit coupling are centered around the modulation of J_w . Here we see that it is also possible to control the effective strength by adjusting the ratio between $|\tilde{t}_w|$ and $|\tilde{s}_w|$. In particular,

when $|\tilde{t}_w| = |\tilde{s}_w|$, no phase difference can accumulate across the bond and the bond can be seen as completely cut off. We note that Δ_w can be interpreted as an effective exchange energy that can take on negative values, in which the energy relation between spin singlet and triplet states are reversed. Such phenomenon have been reported in studies on few-electron coupled quantum dots [70, 71]. We can hence distinguish between the “coupling” and “connectivity” of two dots. Spin on two dots is coupled if the exchange energy J_w is non-zero, while they are considered connected only if the effective coupling strength Δ_w is non-zero. By tuning the relative strength between $|\tilde{t}_w|$ and $|\tilde{s}_w|$ while keeping the exchange energy finite, one can control the connectivity with always-on coupling.

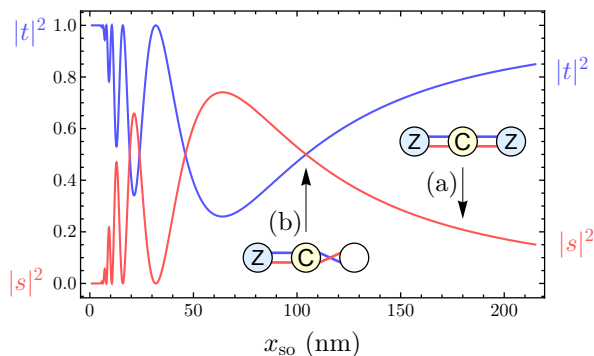


FIG. 8. Dependence of the spin-conserved and spin-flipped tunneling fraction $|\tilde{t}|^2$ and $|\tilde{s}|^2$ on the spin-orbit length x_{SO} for a typical quantum dot array system. The bond connectivity can be controlled by tuning the relative strength between spin-conserved and spin flipped channel. In the subsets, we considered tuning the SOI strength for the right bond in a three-qubit array. We identify the (a) “on” status and (b) “off” status of this bond based on the effective bond strength. This change of status can be achieved even though the coupling energy J remains unchanged.

Experimentally, both \tilde{t}_w and \tilde{s}_w are dependent on the SOI strength and magnetic field angle on the bond w . It is known that the SOI strength can be continuously tuned by varying the electric field strength. Hence for static and global the magnetic field, it is possible to control the SOI strength of a particular bond by changing the local electric field. Extra capacitor structure may be involved to suppress crosstalk and enable such precise control. Current spin qubit devices demonstrating such gate tunability is in [72] and also in [73]. For small SOI coupling $x_{\text{SO}} \gg 2d$, the interdot tunneling is dominated by the spin-conserved process. As the SOI strength increases (x_{SO} decreases), $|\tilde{s}|^2$ picks up and will come across the decreasing $|\tilde{t}|^2$ at some point. This cross point always exists for magnetic field angle $\pi/4 < \vartheta_{\text{B}} < 3\pi/4$ and define the “off” state of the relevant bond. In Fig. 8, we plotted the dependence of $|\tilde{t}|^2$ and $|\tilde{s}|^2$ on the spin-orbit length x_{SO} , for a system with interdot spacing $2d = 100$ nm, characteristic Bohr radius $x_0 = 10$ nm and the an-

gle between magnetic field and SOI vector $\vartheta_{\text{B}} = \pi/3$. Assuming that we are varying the SOI strength for the second bond in a three-qubit array. The insets in Fig. 8 show the intrinsic gates for the (a) “on” state and (b) “off” state of the second bond, where we use parallel lines to indicate a connected bond and cross lines to indicate disconnect bond. In state (a), the effective coupling strengths for the two bonds are identical $\Delta_1 = \Delta_2$, and the qubits experience a CZZ gate after time evolution $\tau = \pi/\Delta_1$. While in state (b), the same time evolution only induces a CZ gate between the left two qubits while leaving the third qubit intact. This property holds for general many-qubit arrays. A particular bond can appear disconnected if the spin-conserved and spin-flipped tunneling strengths are equal.

V. CONCLUSION

This article is a detailed theoretical study of the set of intrinsic multi-qubit gates implemented on spin qubit arrays. Our study involves multiple key aspects such as multi-qubit gate dynamics, fidelity estimation and optimizations, advantages in application, scalable calibration with pulse-protected evolution.

We start out from a general model of a spin qubit chip defined by quantum dot array. To describe the dynamics of the half-filling computational subspace, we adopt an effective Hamiltonian that features representing exchange interaction with entangled states on qubit pairs. The entangled states are associated with tunnel-coupled quantum dots and determined by the spin-conserved and spin-flipped tunneling coefficients, which can be further used to define relevant bond vectors for connecting dots. Using first order perturbation theory, we find the time evolution map in the qubit rotating frame is defined by the grid vector of the quantum dot array, which is the Kronecker sum of all the bond vectors. Intrinsic multi-qubit gates is identified with these rotating frame maps in combination with global and local phase gauges.

Applying the gate composition law to general quantum dot arrays, we identify an important class of gates, multi-qubit controlled phase gates, and show that these gates can be intrinsically achieved by quantum dots arranged in stellar geometry. We then show that all intrinsic multi-qubit gates can be decomposed as simultaneous products of multi-qubit controlled phase gates, and that the local phase correction are determined by the connecting bonds to each dot. We estimate the gate fidelity of these intrinsic gates by deriving an analytical lower bound for the coherent fidelity loss from higher order perturbation terms. It is found that the coherent fidelity is mostly limited by the accumulated phase shifts from second order energy perturbations. The loss in fidelity due to accumulated phase shifts can be effectively suppressed by applying additional local phase corrections obtained from a systematic algorithm. And the fidelity of optimally phase-corrected gates can be further improved by

working in parametric sweet spots of the interdot tunneling coefficients. To showcase the advantages of intrinsic multi-qubit gates, we discuss some examples of their application in quantum error correction code, simultaneous parity measurement and fast array reversal.

Finally, we examine the problem of bond inhomogeneity necessarily encountered by scaling up the system size. We proposed a theoretical scheme in which the bond strengths are dynamically calibrated with fast pulses. After considering specific examples and show its compatibility with dynamical decoupling, we show that such

dynamical calibration protocol can be applied for general array with arbitrary connectivity.

ACKNOWLEDGMENTS

This work is supported by the Beijing Postdoctoral Research Foundation (Grant No. 2023-zz-050) and the National Natural Science Foundation of China (Grant Nos. 92165208 and 11874071).

-
- [1] D. Loss and D. P. DiVincenzo, *Physical Review A* **57**, 120 (1998).
- [2] F. A. Zwanenburg, A. S. Dzurak, A. Morello, M. Y. Simmons, L. C. L. Hollenberg, G. Klimeck, S. Rogge, S. N. Coppersmith, and M. A. Eriksson, *Reviews of Modern Physics* **85**, 961 (2013).
- [3] C. Kloeffel and D. Loss, *Annual Review of Condensed Matter Physics* **4**, 51 (2013).
- [4] G. Burkard, T. D. Ladd, A. Pan, J. M. Nichol, and J. R. Petta, *Reviews of Modern Physics* **95**, 025003 (2023).
- [5] L. M. K. Vandersypen and M. A. Eriksson, *Physics Today* **72**, 38 (2019).
- [6] A. Chatterjee, P. Stevenson, S. De Franceschi, A. Morello, N. P. de Leon, and F. Kuemmeth, *Nature Reviews Physics* **3**, 157 (2021).
- [7] P. Stano and D. Loss, *Nature Reviews Physics* **4**, 672 (2022).
- [8] A. Mills, C. Guinn, M. Feldman, A. Sigillito, M. Gullans, M. Rakher, J. Kerckhoff, C. Jackson, and J. Petta, *Physical Review Applied* **18**, 064028 (2022).
- [9] K. Wang, G. Xu, F. Gao, H. Liu, R.-L. Ma, X. Zhang, Z. Wang, G. Cao, T. Wang, J.-J. Zhang, D. Culcer, X. Hu, H.-W. Jiang, H.-O. Li, G.-C. Guo, and G.-P. Guo, *Nature Communications* **13**, 206 (2022).
- [10] L. C. Camenzind, S. Geyer, A. Fuhrer, R. J. Warburton, D. M. Zumbühl, and A. V. Kuhlmann, *Nature Electronics* **5**, 178 (2022).
- [11] A. Noiri, K. Takeda, T. Nakajima, T. Kobayashi, A. Sammak, G. Scappucci, and S. Tarucha, *Nature* **601**, 338 (2022).
- [12] X. Xue, M. Russ, N. Samkharadze, B. Undseth, A. Sammak, G. Scappucci, and L. M. K. Vandersypen, *Nature* **601**, 343 (2022).
- [13] M. F. Gonzalez-Zalba, S. De Franceschi, E. Charbon, T. Meunier, M. Vinet, and A. S. Dzurak, *Nature Electronics* **4**, 872 (2021).
- [14] A. M. J. Zwerver, T. Krähenmann, T. F. Watson, L. Lampert, H. C. George, R. Pillarisetty, S. A. Bojarski, P. Amin, S. V. Amitonov, J. M. Boter, R. Caudillo, D. Correas-Serrano, J. P. Dehollain, G. Droulers, E. M. Henry, R. Kotlyar, M. Lodari, F. Lüthi, D. J. Michalak, B. K. Mueller, S. Neyens, J. Roberts, N. Samkharadze, G. Zheng, O. K. Zietz, G. Scappucci, M. Veldhorst, L. M. K. Vandersypen, and J. S. Clarke, *Nature Electronics* **5**, 184 (2022).
- [15] N. W. Hendrickx, W. I. L. Lawrie, M. Russ, F. van Riggelen, S. L. de Snoo, R. N. Schouten, A. Sammak, G. Scappucci, and M. Veldhorst, *Nature* **591**, 580 (2021).
- [16] W. I. L. Lawrie, M. Rimbach-Russ, F. van Riggelen, N. W. Hendrickx, S. L. de Snoo, A. Sammak, G. Scappucci, J. Helsen, and M. Veldhorst, *Nature Communications* **14**, 3617 (2023).
- [17] F. Borsoi, N. W. Hendrickx, V. John, M. Meyer, S. Motz, F. van Riggelen, A. Sammak, S. L. de Snoo, G. Scappucci, and M. Veldhorst, *Nature Nanotechnology* **19**, 21 (2024).
- [18] X. Zhang, E. Morozova, M. Rimbach-Russ, D. Jirovec, T.-K. Hsiao, P. C. Fariña, C.-A. Wang, S. D. Oosterhout, A. Sammak, G. Scappucci, M. Veldhorst, and L. M. K. Vandersypen, Universal control of four singlet-triplet qubits (2023), [arXiv:2312.16101](https://arxiv.org/abs/2312.16101) [cond-mat.mes-hall].
- [19] A. Yu. Kitaev, *Annals of Physics* **303**, 2 (2003).
- [20] R. Raussendorf and J. Harrington, *Physical Review Letters* **98**, 190504 (2007).
- [21] A. G. Fowler, M. Mariantoni, J. M. Martinis, and A. N. Cleland, *Physical Review A* **86**, 032324 (2012).
- [22] A. Barenco, C. H. Bennett, R. Cleve, D. P. DiVincenzo, N. Margolus, P. Shor, T. Sleator, J. A. Smolin, and H. Weinfurter, *Physical Review A* **52**, 3457 (1995).
- [23] T. Meunier, V. E. Calado, and L. M. K. Vandersypen, *Physical Review B* **83**, 121403 (2011).
- [24] M. Veldhorst, C. H. Yang, J. C. C. Hwang, W. Huang, J. P. Dehollain, J. T. Muhonen, S. Simmons, A. Laucht, F. E. Hudson, K. M. Itoh, A. Morello, and A. S. Dzurak, *Nature* **526**, 410 (2015).
- [25] T. F. Watson, S. G. J. Philips, E. Kawakami, D. R. Ward, P. Scarlino, M. Veldhorst, D. E. Savage, M. G. Lagally, M. Friesen, S. N. Coppersmith, M. A. Eriksson, and L. M. K. Vandersypen, *Nature* **555**, 633 (2018).
- [26] D. M. Zajac, A. J. Sigillito, M. Russ, F. Borjans, J. M. Taylor, G. Burkard, and J. R. Petta, *Science* **359**, 439 (2018).
- [27] M. Russ, D. M. Zajac, A. J. Sigillito, F. Borjans, J. M. Taylor, J. R. Petta, and G. Burkard, *Physical Review B* **97**, 085421 (2018).
- [28] M. Rimbach-Russ, S. G. J. Philips, X. Xue, and L. M. K. Vandersypen, *Quantum Science and Technology* **8**, 045025 (2023).
- [29] Y.-H. Wu, L. C. Camenzind, A. Noiri, K. Takeda, T. Nakajima, T. Kobayashi, C.-Y. Chang, A. Sammak, G. Scappucci, H.-S. Goan, and S. Tarucha, Hamiltonian phase error in resonantly driven cnot gate above the fault-tolerant threshold (2023), [arXiv:2307.09031](https://arxiv.org/abs/2307.09031) [cond-mat.mes-hall].
- [30] X. Gu, J. Fernández-Pendás, P. Vikstål, T. Abad,

- C. Warren, A. Bengtsson, G. Tancredi, V. Shumeiko, J. Bylander, G. Johansson, and A. F. Kockum, *PRX Quantum* **2**, 040348 (2021).
- [31] L. Isenhower, M. Saffman, and K. Mølmer, *Quantum Information Processing* **10**, 755 (2011).
- [32] M. Khazali and K. Mølmer, *Physical Review X* **10**, 021054 (2020).
- [33] D. Yu, W. Zhang, J. ming Liu, S. Su, and J. Qian, Spheroidal-structure-based multi-qubit toffoli gate via asymmetric rydberg interaction (2020), [arXiv:2007.11938 \[quant-ph\]](https://arxiv.org/abs/2007.11938).
- [34] J. T. Young, P. Bienias, R. Belyansky, A. M. Kaufman, and A. V. Gorshkov, *Physical Review Letters* **127**, 120501 (2021).
- [35] N. Chancellor, S. Zohren, and P. A. Warburton, *npj Quantum Information* **3**, 1 (2017).
- [36] T. Liu, B.-Q. Guo, C.-S. Yu, and W.-N. Zhang, *Optics Express* **26**, 4498 (2018).
- [37] E. Bahnsen, S. Rasmussen, N. Loft, and N. Zinner, *Physical Review Applied* **17**, 024053 (2022).
- [38] S. E. Rasmussen, K. Groenland, R. Gerritsma, K. Schoutens, and N. T. Zinner, *Physical Review A* **101**, 022308 (2020).
- [39] J. D. A. Espinoza, K. Groenland, M. Mazzanti, K. Schoutens, and R. Gerritsma, *Physical Review A* **103**, 052437 (2021), [arxiv:2010.08490 \[quant-ph\]](https://arxiv.org/abs/2010.08490).
- [40] M. J. Gullans and J. R. Petta, *Physical Review B* **100**, 085419 (2019).
- [41] K. Takeda, A. Noiri, T. Nakajima, T. Kobayashi, and S. Tarucha, *Nature* **608**, 682 (2022).
- [42] H. Qiao, Y. P. Kandel, K. Deng, S. Fallahi, G. C. Gardner, M. J. Manfra, E. Barnes, and J. M. Nichol, *Physical Review X* **10**, 031006 (2020).
- [43] H. Qiao, Y. P. Kandel, S. Fallahi, G. C. Gardner, M. J. Manfra, X. Hu, and J. M. Nichol, *Physical Review Letters* **126**, 017701 (2021).
- [44] F. R. Braakman, P. Barthelémy, C. Reichl, W. Wegscheider, and L. M. K. Vandersypen, *Nature Nanotechnology* **8**, 432 (2013).
- [45] J. Knörzer, C. J. van Diepen, T.-K. Hsiao, G. Giedke, U. Mukhopadhyay, C. Reichl, W. Wegscheider, J. I. Cirac, and L. M. K. Vandersypen, *Physical Review Research* **4**, 033043 (2022).
- [46] D. P. DiVincenzo, D. Bacon, J. Kempe, G. Burkard, and K. B. Whaley, *Nature* **408**, 339 (2000).
- [47] J. Levy, *Physical Review Letters* **89**, 147902 (2002).
- [48] Q. Li, Ł. Cywiński, D. Culcer, X. Hu, and S. Das Sarma, *Physical Review B* **81**, 085313 (2010).
- [49] R. E. Throckmorton and S. Das Sarma, *Physical Review B* **103**, 165431 (2021).
- [50] G. X. Chan, P. Huang, and X. Wang, *Physical Review B* **108**, 035402 (2023).
- [51] J. Qi, Z.-H. Liu, and H. Xu, *New Journal of Physics* **26**, 013012 (2024).
- [52] L. Viola, E. Knill, and S. Lloyd, *Physical Review Letters* **82**, 2417 (1999).
- [53] L. Viola, S. Lloyd, and E. Knill, *Physical Review Letters* **83**, 4888 (1999).
- [54] K. Khodjasteh and D. A. Lidar, *Physical Review Letters* **95**, 180501 (2005).
- [55] V. N. Golovach, M. Borhani, and D. Loss, *Physical Review B* **74**, 165319 (2006).
- [56] F. N. M. Froning, L. C. Camenzind, O. A. H. van der Molen, A. Li, E. P. A. M. Bakkers, D. M. Zumbühl, and F. R. Braakman, *Nature Nanotechnology* **16**, 308 (2021).
- [57] E. Kawakami, T. Jullien, P. Scarlino, D. R. Ward, D. E. Savage, M. G. Lagally, V. V. Dobrovitski, M. Friesen, S. N. Coppersmith, M. A. Eriksson, and L. M. K. Vandersypen, *Proceedings of the National Academy of Sciences* **113**, 11738 (2016).
- [58] M. Imada, A. Fujimori, and Y. Tokura, *Reviews of Modern Physics* **70**, 1039 (1998).
- [59] S. Yang, X. Wang, and S. Das Sarma, *Physical Review B* **83**, 161301 (2011).
- [60] R. Li and J. Q. You, *Physical Review B* **90**, 035303 (2014).
- [61] A. Bogan, S. Studenikin, M. Korkusinski, L. Gaudreau, P. Zawadzki, A. S. Sachrajda, L. Tracy, J. Reno, and T. Hargett, *Physical Review Letters* **120**, 207701 (2018).
- [62] L. M. K. Vandersypen, *Rev. Mod. Phys.* **76**, 33 (2004).
- [63] D. C. McKay, C. J. Wood, S. Sheldon, J. M. Chow, and J. M. Gambetta, *Physical Review A* **96**, 022330 (2017).
- [64] M. A. Nielsen, *Physics Letters A* **303**, 249 (2002).
- [65] A. Ben-Israel and T. N. E. Greville, *Generalized Inverses: Theory and Applications* (Krieger, Huntington, N.Y., 1980).
- [66] M. A. Nielsen and I. L. Chuang, *Quantum Computation and Quantum Information*, 10th ed. (Cambridge University Press, Cambridge ; New York, 2010).
- [67] D. Gottesman, *Stabilizer Codes and Quantum Error Correction*, Ph.D. thesis, Caltech (1997), [arxiv:quant-ph/9705052](https://arxiv.org/abs/quant-ph/9705052).
- [68] V. Gimeno and J. M. Sotoca, *Journal of Physics A: Mathematical and Theoretical* **50**, 185302 (2017).
- [69] G.-H. Liang, X.-H. Song, C.-L. Deng, X.-Y. Gu, Y. Yan, Z.-Y. Mei, S.-L. Zhao, Y.-Z. Bu, Y.-X. Xiao, Y.-H. Yu, M.-C. Wang, T. Liu, Y.-H. Shi, H. Zhang, X. Li, L. Li, J.-Z. Wang, Y. Tian, S.-P. Zhao, K. Xu, H. Fan, Z.-C. Xiang, and D.-N. Zheng, Tunable Coupling Architectures with Capacitively Connecting Pads for Large-Scale Superconducting Multi-Qubit Processors (2023), [arxiv:2306.05312 \[quant-ph\]](https://arxiv.org/abs/2306.05312).
- [70] F. Martins, F. K. Malinowski, P. D. Nissen, S. Fallahi, G. C. Gardner, M. J. Manfra, C. M. Marcus, and F. Kuemmeth, *Physical Review Letters* **119**, 227701 (2017).
- [71] K. Deng, F. A. Calderon-Vargas, N. J. Mayhall, and E. Barnes, *Physical Review B* **97**, 245301 (2018).
- [72] S. Bosco, B. Hetényi, and D. Loss, *PRX Quantum* **2**, 010348 (2021).
- [73] H. Liu, T. Zhang, K. Wang, F. Gao, G. Xu, X. Zhang, S.-X. Li, G. Cao, T. Wang, J. Zhang, X. Hu, H.-O. Li, and G.-P. Guo, *Physical Review Applied* **17**, 044052 (2022).
- [74] R. Li, J. Q. You, C. P. Sun, and F. Nori, *Physical Review Letters* **111**, 086805 (2013).
- [75] A. Altland and B. D. Simons, *Condensed Matter Field Theory*, 2nd ed. (Cambridge University Press, 2010).

Appendix A: Computational Hamiltonian

In this section, we outline the basic steps to derive the computational Hamiltonian used in the main text of this paper.

1. Second-quantization form

Our physical setup is an array of N quantum dots working in the half-filling regime. The Hamiltonian of the charge carries can be in general written as

$$H = \sum_{i=1}^N H_1(\mathbf{r}_i) + \sum_{i>j} H_2(\mathbf{r}_i - \mathbf{r}_j), \quad (\text{A1})$$

where H_1 describes a single charge carrier trapped in quantum dots; H_2 is the Coulomb interaction between charge carriers. As the system is kept at low temperature, the physics of interest is captured by the low-energy subspace of the system. We study the low-energy dynamics by isolating a set of low-energy basis states, where H takes on a finite-dimensional representation and the problem can be simplified.

Let us consider deriving a low-energy representation for H_1 . This Hamiltonian can be in general decomposed as

$$H_1 = \frac{1}{2m^*}(\mathbf{p} + q\mathbf{A})^2 + V(\mathbf{r}) + H_{\text{so}}(\mathbf{p}, \boldsymbol{\sigma}) + H_Z(\mathbf{r}), \quad (\text{A2})$$

where m^* is the effective mass according to the envelope function approximation, \mathbf{p} is the canonical momentum, q is the electric charge, \mathbf{A} is the magnetic potential, $V(\mathbf{r})$ is the electrostatic potential of the quantum dot array, H_{so} is the spin-orbit interaction Hamiltonian that couples the carrier momentum \mathbf{p} with its spin $\boldsymbol{\sigma}$, H_Z is the Zeeman energy due to an external magnetic field $\mathbf{B}(\mathbf{r}) = \nabla \times \mathbf{A}$. It is impractical to directly use eigenstates of H_1 as the basis states, as full knowledge of $V(\mathbf{r})$ is required to solve the eigenstates. For our setup, $V(\mathbf{r})$ represents the potential of an array of quantum dots located at $\mathbf{r} = \mathbf{r}_i$ for $i = 1, \dots, N$. We make the physical assumption that the low-energy orbits of H_1 are localized to each dot. That is, for a spinless particle in $V(\mathbf{r})$, the first N eigenstates $|\Phi_i\rangle$ is only prominent in the vicinity of \mathbf{r}_i for $i = 1, \dots, N$. The excited orbital states are energetically well-separated from the ground-state manifold by a characteristic energy $\hbar\Omega$. Formally, we can consider a localized version of Eq. (A2) where the full $V(\mathbf{r})$ is replaced with the local potential $V_i(\boldsymbol{\delta}\mathbf{r}) \approx V(\mathbf{r}_i + \boldsymbol{\delta}\mathbf{r})$, and we associate

$$H_{1,i} = \frac{1}{2m^*}(\mathbf{p} + q\mathbf{A})^2 + V_i(\mathbf{r}) + H_{\text{so}}(\mathbf{p}, \boldsymbol{\sigma}) + H_Z(\mathbf{r}), \quad \text{for } i = 1, \dots, N. \quad (\text{A3})$$

In the absence of the Zeeman term H_Z , this Hamiltonian is symmetric under time-reversal. The Kramer degeneracy is lifted with a finite \mathbf{B} -field that picks up a preferred quantization axis for each dot. We denote the eigenstates of $H_{1,i}$ at $\mathbf{B} = 0$ as $|\phi_{in\sigma}^{(0)}\rangle$, with the dot index $i = 1, \dots, N$, the orbital index $n = 0, 1, \dots, \infty$, and the spin index $\sigma = \uparrow, \downarrow$ (for a pre-defined z -direction). The eigenstates $\{|\phi_{in\sigma}^{(0)}\rangle\}$ are fully solvable: by making a translating in momentum, we can reduce $H_{1,i}$ to $H'_{1,i} = \frac{\mathbf{p}^2}{2m^*} + V_i(\mathbf{r})$, whose solutions are elementary. Analytical solution to the eigenstates of (A3) can be derived perturbatively under the assumption that $\xi_Z \equiv E_Z/\hbar\Omega \ll 1$, where $E_Z \propto |\mathbf{B}|$ is the characteristic Zeeman energy splitting of the charge carriers. In general, we can write the ground-level eigenstates of $H_{1,i}$ as

$$|\phi_{i\sigma}\rangle = c_{0\sigma}|\phi_{i0\uparrow}^{(0)}\rangle + d_{0\sigma}|\phi_{i0\downarrow}^{(0)}\rangle + \sum_{n=1}^{\infty} \xi_Z \left(c_{n\sigma}|\phi_{in\uparrow}^{(0)}\rangle + d_{n\sigma}|\phi_{in\downarrow}^{(0)}\rangle \right) + O(\xi_Z^2), \quad (\text{A4})$$

where $c_{n\sigma}, d_{n\sigma}$ are coefficients that decreases sub-exponentially with n . Furthermore, the quantization energy between $|\phi_{i\uparrow}\rangle$ and $|\phi_{i\downarrow}\rangle$ is modified to a reduced value $\varepsilon_{Z,i} < E_{Z,i}$. Detailed expressions to $c_{n\sigma}$ and $d_{n\sigma}$ can be found by assuming a particular form of the local potential $V_i(\mathbf{r})$ and H_{so} . For example, Ref. 74 contains the expression for the case of Harmonic potential and Rashba spin-orbit interaction. Here we are not concerned with the details, apart from the knowledge that $c_{n\sigma}$ and $d_{n\sigma}$ are independent of the magnetic field magnitude $|\mathbf{B}|$ (but they do dependent on the field angle).

Assuming that we have solved the ground-level eigenstates in Eq. (A4), we can use these ‘‘dot-local’’ states to constructs a low-energy basis for our problem. This basis can be obtained by performing orthogonalization among the local states, resulting in the following set of basis states for the 2^N -dimensional low-energy manifold

$$\left\{ |\Phi_{i\sigma}\rangle := \sum_{j=1}^N \sum_{\sigma'=\uparrow,\downarrow} f_{i\sigma,j\sigma'} |\phi_{j\sigma'}\rangle \right\}, \quad (\text{A5})$$

where the coefficients $f_{i\sigma,j\sigma'}$ can be determined with a systematic orthogonalization procedure. Here, we need not be concerned with full expressions of these coefficients, apart from the premise that there is a symmetric procedure of orthogonalization that satisfies $f_{i\sigma,i\sigma} \sim 1$ and $f_{i\sigma,j\sigma'} \sim -2^{-N/2} \langle \phi_{i\sigma} | \phi_{j\sigma'} \rangle$ to the leading order smallness in wave function overlaps.

With the low-energy basis states defined, we can associate the creation $a_{i\sigma}^\dagger$, annihilation operators $a_{i\sigma}$ and the number operator $n_{j\sigma} = a_{j\sigma}^\dagger a_{j\sigma}$ for the state $|\Phi_{i\sigma}\rangle$. Using these field operators, the low-energy Hamiltonian can be brought into second-quantized form [75],

$$H = \underbrace{\sum_j \sum_\sigma (\varepsilon_{j\sigma} n_{j\sigma} + \frac{1}{2} U_j n_{j\sigma} n_{j\bar{\sigma}})}_{H_d} + \underbrace{\sum_{\langle j,k \rangle} \sum_\sigma (t_{\sigma\sigma'}^{jk} a_{j\sigma}^\dagger a_{k\sigma} + t_{\sigma\bar{\sigma}}^{jk} a_{j\sigma}^\dagger a_{k\bar{\sigma}})}_{H_t}. \quad (\text{A6})$$

We interpreted the first and second term as the dot Hamiltonian H_d and the tunneling Hamiltonian H_t respectively. The summation for $\langle j,k \rangle$ in H_t is only performed for direction connected pair of quantum dots j and k . The coefficients in Eq. (A6) are obtained by calculating the matrix elements of H under the basis states. In particular,

$$\varepsilon_{j\sigma} = \mu_j + \text{sig}(\sigma_j) \frac{1}{2} \varepsilon_{Z,j}, \quad (\text{A7})$$

is the energy associated with the state $|\Phi_{j\sigma}\rangle$ that depends on the chemical potential μ_j and effective Zeeman energy $\varepsilon_{Z,j}$ at dot j , with $\text{sig}(\uparrow\downarrow) = \pm 1$. U_j is the Coulomb energy cost for filling two antiparallel spins into the same dot j . The tunneling coefficients in H_t are given by the off-diagonal matrix elements $t_{\sigma\sigma'}^{jk} \equiv \langle \Phi_{j\sigma} | H_1 | \Phi_{k\sigma'} \rangle$. By previous construction, we can split H_1 into a local Hamiltonian in addition to a potential difference $H_1 = H_{1,j} + \Delta V_j = H_{1,k} + \Delta V_k \equiv \frac{1}{2}(H_{1,j} + H_{1,k}) + \Delta V_{jk}$. Therefore the tunneling coefficients can be approximated by

$$\begin{aligned} t_{\sigma\sigma'}^{jk} &= \frac{1}{2} \langle \Phi_{j\sigma} | H_{1,j} | \Phi_{k\sigma'} \rangle + \frac{1}{2} \langle \Phi_{j\sigma} | H_{1,k} | \Phi_{k\sigma'} \rangle + \langle \Phi_{j\sigma} | \Delta V_{jk} | \Phi_{k\sigma'} \rangle \\ &\approx \langle \phi_{j\sigma} | \phi_{k\sigma'} \rangle \left(-\frac{1}{2} \varepsilon_{j\sigma} + \frac{1}{2} \varepsilon_{k\sigma'} + v_{jk} \right), \end{aligned} \quad (\text{A8})$$

where v_{jk} is the characteristic barrier energy between the dots. A more detailed derivation of this result can be found in the appendix of [51] for the case of double-dot.

2. Tunneling coefficients and weak time-reversal symmetry

To establish an additional set of relation between the tunneling coefficients, we require the system to satisfy a weak time-reversal symmetry condition.

Let us consider the time-reversal operator $\hat{T} = -i\sigma_y \hat{K}$, where \hat{K} is the complex conjugation operator for orbital wave functions. Its action on the field operators can be summarized as $\hat{T} a_{j\uparrow} \hat{T}^\dagger = a_{j\downarrow}$, $\hat{T} a_{j\downarrow}^\dagger \hat{T}^\dagger = a_{j\uparrow}^\dagger$, $\hat{T} a_{j\downarrow} \hat{T}^\dagger = -a_{j\uparrow}$ and $\hat{T} a_{j\uparrow}^\dagger \hat{T}^\dagger = -a_{j\downarrow}^\dagger$. Examining the second-quantized Hamiltonian Eq. (A6), we see that H_d directly violate the time-reversal symmetry due to the sign reversal before $\varepsilon_{Z,j}$,

$$\hat{T} H_d \hat{T}^\dagger = \sum_{j\sigma} [(\mu_j - \text{sig}(\sigma_j) \frac{1}{2} \varepsilon_{Z,j}) n_{j\sigma} + \frac{1}{2} U n_{j\sigma} n_{j\bar{\sigma}}] \neq H_d \quad (\text{A9})$$

This is expected naturally as an external magnetic field breaks time-reversal symmetry.

For H_t , we make the assumption that the interdot tunneling coefficients are independent of the external magnetic field strength

$$\frac{\partial}{\partial |\mathbf{B}|} t_{\sigma\sigma'}^{jk} \approx 0. \quad (\text{A10})$$

We justify this assumption by examining Eq. (A8). First, the local states $|\phi_{j\sigma}\rangle$ and $|\phi_{k\sigma'}\rangle$ are independent of $|\mathbf{B}|$ up to the first order according to Eq. (A4). Next, the interdot barrier energy is much larger than the Zeeman energy difference $v_{jk} \gg \varepsilon_{Z,k} - \varepsilon_{Z,j}$ in typical systems, such that the later contributes negligibly to the tunneling rate and we can approximate $t_{\sigma\sigma'}^{jk} \approx \langle \phi_{j\sigma} | \phi_{k\sigma'} \rangle v_{jk}$, which is invariant under $|\mathbf{B}|$. Now, combining Eq. (A10) with the fact that a closed system satisfies time reversal symmetry at zero external magnetic field $\mathbf{B} = 0$, it follows that H_t must be invariant under time reversal $H_t = \hat{T} H_t \hat{T}^\dagger$. We refer this property of H_t as the weak time-reversal symmetry condition.

Comparing the normal tunneling Hamiltonian with the time-reversed tunneling Hamiltonian,

$$\begin{aligned} H_t &= \sum_{\langle j,k \rangle} \left(t_{\uparrow\uparrow}^{jk} a_{j\uparrow}^\dagger a_{k\uparrow} + t_{\downarrow\downarrow}^{jk} a_{j\downarrow}^\dagger a_{k\downarrow} + t_{\uparrow\downarrow}^{jk} a_{j\uparrow}^\dagger a_{k\downarrow} + t_{\downarrow\uparrow}^{jk} a_{j\downarrow}^\dagger a_{k\uparrow} + h.c. \right), \\ \widehat{T} H_t \widehat{T}^\dagger &= \sum_{\langle j,k \rangle} \left((t_{\uparrow\uparrow}^{jk})^* a_{j\downarrow}^\dagger a_{k\downarrow} + (t_{\downarrow\downarrow}^{jk})^* a_{j\uparrow}^\dagger a_{k\uparrow} - (t_{\uparrow\downarrow}^{jk})^* a_{j\downarrow}^\dagger a_{k\uparrow} - (t_{\downarrow\uparrow}^{jk})^* a_{j\uparrow}^\dagger a_{k\downarrow} + h.c. \right), \end{aligned} \quad (\text{A11})$$

we can equate

$$t_{\uparrow\uparrow}^{jk} = (t_{\downarrow\downarrow}^{jk})^*, \quad t_{\uparrow\downarrow}^{jk} = (t_{\downarrow\uparrow}^{jk})^*, \quad t_{\downarrow\downarrow}^{jk} = -(t_{\uparrow\uparrow}^{jk})^*, \quad t_{\downarrow\uparrow}^{jk} = -(t_{\uparrow\downarrow}^{jk})^*. \quad (\text{A12})$$

Another set of relation follows from the Hermiticity of H_t ,

$$t_{\uparrow\uparrow}^{jk} = (t_{\uparrow\uparrow}^{kj})^*, \quad t_{\downarrow\downarrow}^{jk} = (t_{\downarrow\downarrow}^{kj})^*, \quad t_{\uparrow\downarrow}^{jk} = (t_{\uparrow\downarrow}^{kj})^*, \quad t_{\downarrow\uparrow}^{jk} = (t_{\downarrow\uparrow}^{kj})^*. \quad (\text{A13})$$

Combining these two sets of relations, it follows that there are only two independent tunneling coefficients, representing the spin-conserved and spin-flipped processes respectively

$$\begin{aligned} t_{\uparrow\uparrow}^{jk} &= (t_{\downarrow\downarrow}^{jk})^* = t_{\downarrow\downarrow}^{kj} = (t_{\uparrow\uparrow}^{kj})^* \equiv t_{jk} \\ t_{\uparrow\downarrow}^{jk} &= -(t_{\downarrow\uparrow}^{jk})^* = -t_{\downarrow\uparrow}^{kj} = (t_{\downarrow\uparrow}^{kj})^* \equiv s_{jk}. \end{aligned} \quad (\text{A14})$$

Therefore we can reduce the tunneling Hamiltonian to

$$H_t = \sum_{\langle j,k \rangle} \left(t_{jk} a_{j\uparrow}^\dagger a_{k\uparrow} + t_{jk}^* a_{j\downarrow}^\dagger a_{k\downarrow} + s_{jk} a_{j\uparrow}^\dagger a_{k\downarrow} - s_{jk}^* a_{j\downarrow}^\dagger a_{k\uparrow} + h.c. \right) \quad (\text{A15})$$

3. Computational Hamiltonian

Till now, we have been working with single-body wave functions. To describe the dynamics with multiple spin qubits, we must derive a matrix representation of the low-energy Hamiltonian Eq. (A6) using multi-body basis states. These states are anti-symmetrized product states of the single-body wave functions in (A5). For example, a system of three quantum dots all in the spin-up state is specified by the antisymmetric wave function:

$$|\uparrow\uparrow\uparrow\rangle = \widehat{A} \left(|\Phi_{1\uparrow}\rangle |\Phi_{2\uparrow}\rangle |\Phi_{3\uparrow}\rangle \right) = \frac{1}{\sqrt{3!}} \begin{vmatrix} |\Phi_{1\uparrow}\rangle_1 & |\Phi_{2\uparrow}\rangle_1 & |\Phi_{3\uparrow}\rangle_1 \\ |\Phi_{1\uparrow}\rangle_2 & |\Phi_{2\uparrow}\rangle_2 & |\Phi_{3\uparrow}\rangle_2 \\ |\Phi_{1\uparrow}\rangle_3 & |\Phi_{2\uparrow}\rangle_3 & |\Phi_{3\uparrow}\rangle_3 \end{vmatrix}, \quad (\text{A16})$$

where \widehat{A} denotes the antisymmetrization operator; the subscripts for kets in the Slater determinant explicitly label the charge carriers. But such notation is irrelevant after antisymmetrization. By considering all combinations of single body wave functions, we also allow two charge carriers occupying the same dot. Restricting to the ground orbital states, the only possibilities are that of antiparallel states within a dot. We denote such state using the letter 'S' in suggestion of a singlet state. But the actual wave function differ from a plain singlet as the antisymmetrization is performed over all fermions instead of just two. For example, we define the shorthand

$$|0S\uparrow\rangle = \widehat{A} \left(|\Phi_{2\uparrow}\rangle |\Phi_{2\downarrow}\rangle |\Phi_{3\uparrow}\rangle \right) = \frac{1}{\sqrt{3!}} \begin{vmatrix} |\Phi_{2\uparrow}\rangle_1 & |\Phi_{2\downarrow}\rangle_1 & |\Phi_{3\uparrow}\rangle_1 \\ |\Phi_{2\uparrow}\rangle_2 & |\Phi_{2\downarrow}\rangle_2 & |\Phi_{3\uparrow}\rangle_2 \\ |\Phi_{2\uparrow}\rangle_3 & |\Phi_{2\downarrow}\rangle_3 & |\Phi_{3\uparrow}\rangle_3 \end{vmatrix}, \quad (\text{A17})$$

where the label '0' indicates that the first dot is unoccupied. In the followings, we will assume all such multi-body states are defined in such antisymmetric manner.

The states in Eq. (A16) and Eq. (A17) are examples of the half-filling states and doubly-occupied states. Splitting the multi-body wave function basis according to the half-filling states and the doubly-occupied states, the Hamiltonian carries the following representation in the combined Hilbert space

$$H = \left[\begin{array}{c|c} \begin{matrix} \ddots & & \\ & H_{\text{low}} & \\ & & \ddots \end{matrix} & \begin{matrix} T^\dagger \\ \\ \end{matrix} \\ \hline \begin{matrix} T \\ \\ \end{matrix} & \begin{matrix} \ddots & & \\ & H_{\text{high}} & \\ & & \ddots \end{matrix} \end{array} \right] \left. \begin{array}{l} \text{half-filling states} \\ \text{doubly-occupied states} \end{array} \right\}, \quad (\text{A18})$$

to bring the Hamiltonian in Eq. (A18) into block-diagonal form, and the computational Hamiltonian is defined by $H_{\text{comp}} = \mathcal{P}e^S H e^{-S}$, where \mathcal{P} is the projection operator on the half-filling subspace. Assuming $H = H_0 + V$, where

$$H_0 = \begin{bmatrix} H_{\text{low}} & 0 \\ 0 & H_{\text{high}} \end{bmatrix}, \quad V = \begin{bmatrix} 0 & T^\dagger \\ T & 0 \end{bmatrix} \quad (\text{A25})$$

represents the diagonal and off-diagonal blocks of the full H in Eq. (A18). An matrix S that satisfies $[H_0, S] = V$ can transform the Hamiltonian into block-diagonal form up to the fourth order, giving

$$H_{\text{comp}} = H_{\text{low}} + \mathcal{P} \frac{1}{2} [S, V] + O((t/U)^4), \quad (\text{A26})$$

where t and U stands for the characteristic tunneling energy and on-site Coulomb charging energy. The ratio between the two is assumed very small such that the first two terms give an accurate depiction of the computation Hamiltonian. As the first term is already derive in Eq. (A21), the goal is to derive a suitable expression for the second term. As the diagonal block H_0 is in fact fully diagonal, we can explicit construct S by its elements

$$S_{ii} = 0, \quad S_{ij} = \frac{V_{ij}}{(H_0)_{ii} - (H_0)_{jj}} \quad (i \neq j). \quad (\text{A27})$$

One can obtain out the resulting Hamiltonian by substituting in expressions for H_0 and V .

Let us consider the triple-dot chain example. The V matrix is already specified by the the off-diagonal block in Eq. (A24). Under the same ordering of basis states, we also have the low-energy diagonal block

$$H_{\text{low}} = \frac{1}{2} \text{diag}(\varepsilon_1^Z + \varepsilon_2^Z + \varepsilon_3^Z, \varepsilon_1^Z + \varepsilon_2^Z - \varepsilon_3^Z, \varepsilon_1^Z - \varepsilon_2^Z + \varepsilon_3^Z, \varepsilon_1^Z - \varepsilon_2^Z - \varepsilon_3^Z, \\ -\varepsilon_1^Z + \varepsilon_2^Z + \varepsilon_3^Z, -\varepsilon_1^Z + \varepsilon_2^Z - \varepsilon_3^Z, -\varepsilon_1^Z - \varepsilon_2^Z + \varepsilon_3^Z, -\varepsilon_1^Z - \varepsilon_2^Z - \varepsilon_3^Z), \quad (\text{A28})$$

and the low-energy diagonal block

$$H_{\text{high}} = \text{diag}(U_1 + \mu_1 - \mu_2 + \frac{1}{2}\varepsilon_3^Z, U_1 + \mu_1 - \mu_2 - \frac{1}{2}\varepsilon_3^Z, U_2 - \mu_1 + \mu_2 + \frac{1}{2}\varepsilon_3^Z, U_2 - \mu_1 + \mu_2 - \frac{1}{2}\varepsilon_3^Z, \\ U_2 + \mu_2 - \mu_3 + \frac{1}{2}\varepsilon_1^Z, U_3 - \mu_2 + \mu_3 + \frac{1}{2}\varepsilon_1^Z, U_2 + \mu_2 - \mu_3 - \frac{1}{2}\varepsilon_1^Z, U_3 - \mu_2 + \mu_3 - \frac{1}{2}\varepsilon_1^Z). \quad (\text{A29})$$

Using computer algebra program, we can explicitly work out the commutator, which can be decomposed as

$$\mathcal{P} \frac{1}{2} [S, V] = H_{\text{ex},12} \otimes I_3 + I_1 \otimes H_{\text{ex},23}, \quad (\text{A30})$$

where $H_{\text{ex},12}$ and $H_{\text{ex},23}$ are four-dimensional matrices on the subspace of the qubit-pair 1,2 and 2,3 respectively; I_1 and I_3 are identity matrices on qubit-1 and qubit-3 subspace. The matrix elements of $H_{\text{ex},12}$ is explicitly given by

$$(H_{\text{ex},12})_{ij} = -\frac{1}{2} (\mathbf{j}_{12,i} + \mathbf{j}_{12,j}) \boldsymbol{\xi}_{12,i} \boldsymbol{\xi}_{12,j}^*, \quad (\text{A31})$$

for the vector \mathbf{j}_{12} defined by

$$\begin{aligned} j_{12,1} &= \frac{1}{U_1 + \mu_1 - \mu_2 - \varepsilon_1^Z/2 - \varepsilon_2^Z/2} + \frac{1}{U_2 + \mu_2 - \mu_1 - \varepsilon_1^Z/2 - \varepsilon_2^Z/2} \\ j_{12,2} &= \frac{1}{U_1 + \mu_1 - \mu_2 - \varepsilon_1^Z/2 + \varepsilon_2^Z/2} + \frac{1}{U_2 + \mu_2 - \mu_1 - \varepsilon_1^Z/2 + \varepsilon_2^Z/2} \\ j_{12,3} &= \frac{1}{U_1 + \mu_1 - \mu_2 + \varepsilon_1^Z/2 - \varepsilon_2^Z/2} + \frac{1}{U_2 + \mu_2 - \mu_1 + \varepsilon_1^Z/2 - \varepsilon_2^Z/2} \\ j_{12,4} &= \frac{1}{U_1 + \mu_1 - \mu_2 - \varepsilon_1^Z/2 - \varepsilon_2^Z/2} + \frac{1}{U_2 + \mu_2 - \mu_1 + \varepsilon_1^Z/2 + \varepsilon_2^Z/2}, \end{aligned} \quad (\text{A32})$$

and the vector $\boldsymbol{\xi}_{12} \equiv (s_1, -t_1, t_1^*, s_1^*)$. As the Zeeman energy ε^Z is small compared to both U and μ , the four components in Eq. (A32) are almost identical to each other. It is customary to introduce the exchange energy between dot 1,2 by

$$J_{12} \equiv \frac{(|s_1|^2 + |t_1|^2)}{2} \left(\frac{1}{U_1 + \mu_1 - \mu_2} + \frac{1}{U_2 + \mu_2 - \mu_1} \right). \quad (\text{A33})$$

Then we can simply the exchange Hamiltonian into

$$H_{\text{ex},12} \simeq -J_{12}|\xi_{12}\rangle\langle\xi_{12}|, \quad (\text{A34})$$

for the entangled state defined on the Hilbert space of dot 1,2 by

$$\begin{aligned} |\xi_{12}\rangle &\propto s_1|\uparrow\uparrow\rangle_{12} - t_1|\uparrow\uparrow\rangle_{12} + t_1^*|\uparrow\uparrow\rangle_{12} + s_1^*|\uparrow\uparrow\rangle_{12} \\ &\equiv \frac{1}{\sqrt{2}} (\tilde{s}_1|\uparrow\uparrow\rangle_{12} - \tilde{t}_1|\uparrow\uparrow\rangle_{12} + \tilde{t}_1^*|\uparrow\uparrow\rangle_{12} + \tilde{s}_1^*|\uparrow\uparrow\rangle_{12}), \end{aligned} \quad (\text{A35})$$

for the dimensionless and normalized tunneling coefficients \tilde{s} and \tilde{t} satisfying $|\tilde{s}_1|^2 + |\tilde{t}_1|^2 = 1$. The other exchange Hamiltonian $H_{\text{ex},23}$ is defined similarly, with the replacement of pair 1,2 with pair 2,3. This lead to the total exchange Hamiltonian

$$H_{\text{ex}} = -J_{12}|\xi_{12}\rangle\langle\xi_{12}| - J_{23}|\xi_{23}\rangle\langle\xi_{23}|. \quad (\text{A36})$$

This result for triple-dot chain extends our earlier work for double-dot system [51], and inspires us to formulate a more general form of the exchange Hamiltonian for an arbitrary array of quantum dots

$$H_{\text{ex}} = -\sum_w J_w|\xi_w\rangle\langle\xi_w|, \quad (\text{A37})$$

where the summation index w ranges over all pairs of directly connected quantum dots. Both the exchange energy J_w and the state $|\xi_w\rangle$ are defined similarly as in Eq. (A33) and Eq. (A35). That is, we attach entangled states for every connecting bonds of the array, and sum up all the exchange Hamiltonian independently.

We can prove this conjecture (A37) by examining the steps that leads to (A36). The key observation is that the tunneling coefficients for different bonds correspond to different matrix elements in distinctive matrix blocks. Therefore we can split the V and S matrix by

$$V = \sum_w V_w, \quad S = \sum_w S_w, \quad (\text{A38})$$

where V_w consists of only elements proportional to s_w or t_w , and S_w is defined by V_w according to Eq. (A27). Specifically, we can represent V_w by

$$V_w = \sum_{n,j} v_{n,j}^w |\Omega_{n,j}^w\rangle\langle n| + h.c., \quad (\text{A39})$$

where $|n\rangle$ is from the set of half-filling states and $|\Omega_{n,j}^w\rangle$ is from the set of doubly-occupied states, $v_{n,j}^w$ is proportional to the tunneling coefficient s_w or t_w . As different tunneling process maps $|n\rangle$ to different doubly-occupied states, we have

$$\langle\Omega_{n,j}^w|\Omega_{m,k}^v\rangle \propto \delta_{wv}. \quad (\text{A40})$$

As S_w is defined element-wise by V_w , we also have the representation

$$S_w = \sum_{n,j} s_{n,j}^w |\Omega_{n,j}^w\rangle\langle n| + h.c., \quad (\text{A41})$$

for some complex coefficient $s_{n,j}^w$. It is now straightforward to verify that

$$\mathcal{P}S_wV_v = \mathcal{P}V_vS_w = \mathcal{P}[S_w, V_v] = 0 \quad \text{for } w \neq v. \quad (\text{A42})$$

A consequence for this commutativity is that the full basis rotation for the Schrieffer-Wolff transformation is now decomposed into successive rotations responsible for the tunneling coefficients for each connecting bonds. As each pair of commutator for S_w and V_w can be worked out in the subspace of the pair w , which is already solved for the double-dot case, we have

$$H_{\text{ex}} = \sum_{w,v} \mathcal{P}\frac{1}{2}[S_w, V_v] = \sum_w \mathcal{P}\frac{1}{2}[S_w, V_w] = -\sum_w J_w|\xi_w\rangle\langle\xi_w|. \quad (\text{A43})$$

This completes our proof.

Appendix B: Gate Fidelity estimation

To derive the (average) gate fidelity, we use the formula

$$F(\tilde{U}, \tilde{U}_{\text{ideal}}) = \frac{d + |\text{tr}(\tilde{U}^\dagger \tilde{U}_{\text{ideal}})|^2}{d(d+1)}, \quad (\text{B1})$$

where d is the dimension of the system Hilbert space. While \tilde{U} has non-diagonal elements in the computational basis $\{|n\rangle\}$, the \tilde{U}_{ideal} gate is diagonal in the same basis,

$$\tilde{U}_{\text{ideal}} = \text{diag}(e^{-i\tau\delta E_1^{(1)}}, e^{-i\tau\delta E_2^{(1)}}, \dots, e^{-i\tau\delta E_d^{(1)}}). \quad (\text{B2})$$

Hence only the diagonal elements of \tilde{U} contribute to the gate fidelity. The diagonal elements of the uncorrected gate are given by

$$\begin{aligned} \langle n | \tilde{U}(\tau) | n \rangle &= \langle n | e^{i\tau H_0} e^{-i\tau H} | n \rangle = \left\langle n \left| e^{i\tau E_n} \sum_m e^{-i\tau E'_m} |m'\rangle \langle m'| \right| n \right\rangle \\ &= \sum_m r_{nm} e^{-i\tau(E'_{mn} + \delta E_n)}, \end{aligned} \quad (\text{B3})$$

with $r_{nm} = |\langle n | m' \rangle|^2$, $\delta E_n \equiv E'_n - E_n$ and $E'_{mn} \equiv E'_m - E'_n$. We can calculate the trace product between \tilde{U}_{ideal} and \tilde{U} by

$$\left| \text{tr}(\tilde{U}^\dagger \tilde{U}_{\text{ideal}}) \right| = \left| \sum_{n,m} r_{nm} e^{-i(\tau E'_{mn} + \varphi_n)} \right|, \quad (\text{B4})$$

where we define $E'_{mn} \equiv E'_m - E'_n$ and the residue phases $\varphi_n \equiv \tau(\delta E_n - \delta E_n^{(1)})$. As \tilde{U}_{ideal} represents a typical quantum gate, it is expected that $|\tau\delta E_n^{(1)}| = O(1)$ and $|\varphi_n| \simeq |\tau\delta E_n^{(2)}| \ll 1$. If only first order perturbation is considered, we have $r_{nm} \approx \delta_{nm}$ and $\varphi_n \approx 0$, which produce d for the trace product in Eq. (B4) and unit gate fidelity. Therefore, the coherent error rate is of second order in the perturbative strength.

To study the contributing factors of the coherent gate error, we now explicitly derive a lower bound of the gate fidelity. For easier characterization of the coherent error strength, it is better to adopt the gate infidelity $\text{InF} = 1 - F$ and derive an upper bound for it. Setting $|\text{tr}(\tilde{U}^\dagger \tilde{U}_{\text{ideal}})| = d - \epsilon$ for a small deviation $\epsilon \geq 0$, we have

$$\text{InF} = \frac{d^2 - (d - \epsilon)^2}{d^2 + d} \leq \frac{2}{d+1} \epsilon. \quad (\text{B5})$$

To bound ϵ , we consider the following bound for the trace product

$$\begin{aligned} d - \epsilon &= \left| \sum_n [r_{nn} e^{-i\varphi_n} + \sum_{m \neq n} r_{nm} e^{-i(\tau E'_{mn} + \varphi_n)}] \right| \\ &\geq \left| \sum_n [r_{nn} \cos \varphi_n + \sum_{m \neq n} r_{nm} \cos(\tau E'_{mn} + \varphi_n)] \right| \\ &\geq \left| \sum_n [r_{nn} \cos \varphi_n - (1 - r_{nn})] \right| \\ &\geq d - 2 \sum_n (1 - r_{nn}) - \frac{1}{2} \sum_n \varphi_n^2, \end{aligned} \quad (\text{B6})$$

where we have used $|z| \geq |\text{Re} z|$ for the first inequality; the perturbative assumption that $r_{nn} \lesssim 1$ and $r_{nm} \gtrsim 0$ for $m \neq n$, together with the normalization property $\sum_m r_{nm} = 1$ for the second inequality; the trig inequality $\cos \varphi_n \geq 1 - \frac{1}{2} \varphi_n^2$ together with $r_{nn} \leq 1$ for the third inequality. This leads to the final infidelity upper bound

$$\text{InF} \leq \frac{4}{d+1} \sum_n (1 - r_{nn}) + \frac{1}{d+1} \sum_n \varphi_n^2, \quad (\text{B7})$$

appearing in the main text.